A Pooled CRISPR-Based Neuronal Activity Screen Links TMEM50A-Dependent MVB Function to Synaptic Integrity and Remote Memory

Jianhui Wang[1,2,5], Meiqi Liu[3,4,5], Yiming Chen[1,2,5], Jiancheng Chen[3,4], Xin Zhong[1,2], Zilong Wang[1,2,*], Xian Jiang[3,4,*], Ruilin Tian[1,2,*]

[1]SUSTech Homeostatic Medicine Institute, Department of Medical Neuroscience, School of Medicine, Southern University of Science and Technology, Shenzhen 518055, China

[2]Key University Laboratory of Metabolism and Health of Guangdong, Southern University of Science and Technology, Shenzhen 518055, China

[3]Institute of Neurological and Psychiatric Disorders, Shenzhen Bay Laboratory, Shenzhen 518132, China

[4]School of Chemical Biology and Biotechnology, Peking University Shenzhen Graduate School, Shenzhen 518055, China

[5]These authors contributed equally

[*]Correspondence: wangzl6@sustech.edu.cn (Z.W.), jiangxian@szbl.ac.cn (X.J.) and tianrl@sustech.edu.cn (R.T.)

SUMMARY

While advances in omics profiling have rapidly expanded the catalog of genes associated with brain activity in health and disease, functional annotation has lagged far behind. Here, we establish a high-throughput functional genomics platform that couples the

calcium-integrating sensor CaMPARI2 with CRISPRi screening in human iPSC-derived neurons. By converting cumulative neuronal activity into a stable, flow cytometry–readable signal, this approach enables systematic interrogation of neuronal activity through pooled screening. Using a focused library of memory-associated genes, we recover known regulators and identify TMEM50A, a previously uncharacterized protein, as an essential regulator for neuronal activity. TMEM50A forms a complex with LEPROTL1 and associates with ESCRT-III machinery on multivesicular bodies (MVBs). TMEM50A loss impairs MVB function, remodels the neuronal surface proteome, reduces synapse density, and alters behavior in mice. This platform enables systematic discovery of neuronal activity regulators and reveals a critical role for TMEM50A-dependent MVB function in maintaining synaptic integrity and behavior.

INTRODUCTION

Neuronal activity is a unique physiological property of neurons, fundamental to their function and tightly regulated to support behavior. Its dysregulation contributes to diverse neurological diseases, including epilepsy[1] , neurodegenerative diseases[2] , and neurodevelopmental disorders[3,4] . Neuronal activity is shaped by the intrinsic excitability of individual neurons and by their synaptic connectivity and strength within neural circuits. Although many key regulators have been identified, including ion channels[5–8] , synaptic assembly factors[9] and transcriptional and post-translational modulators[10,11] , the molecular mechanisms controlling neuronal activity remain incompletely characterized and lack systematic investigation.

Rapid advances in omics profiling technologies have greatly expanded the scale of candidate gene discovery linked to behavior-associated neuronal activity. For example, single-cell transcriptomics have revealed hundreds to thousands of differentially expressed genes (DEGs) in neurons that are active during learning and memory[12–15] . However, a major challenge is to move beyond expression correlations to pinpoint genes, from these long candidate lists, that causally regulate neuronal activity and behavior, and to define the molecular and cellular mechanisms through which they act.

Systematic identification of genes regulating neuronal activity has been hindered by the lack of high-throughput screening tools for neuronal activity phenotypes. Patch-clamp electrophysiology

provides gold-standard measurements but is technically demanding and low-throughput[16,17] . Voltage and calcium imaging with chemical or genetically encoded probes offer optical readout of neuronal activity but capture transient, dynamic signals that require real-time monitoring with fluorescence microscopy or microplate readers[18–20] , constraining throughput to low- or medium-scale arrayed formats (Figure 1A).

CaMPARI (Calcium-Modulated Photoactivatable Ratiometric Integrator) offers an alternative strategy for calcium-based neuronal activity detection[21–24] . Unlike real-time calcium indicators. CaMPARI is a calcium integrator, capable of recording cumulative calcium activity over defined time periods. Under conditions of elevated intracellular calcium, coincident illumination with violet light induces irreversible photoconversion of CaMPARI from green to red fluorescence. This property enables the conversion of neuronal activity—which is accompanied by Ca^{2+} influx—during a defined illumination window into a stable, integrated fluorescence parameter: the red-to-green (R/G) ratio. CaMPARI has thus been adopted for *in vivo* labeling of behaviorally relevant neuronal ensembles[25,26] .

Here, we leveraged CaMPARI's unique ability to convert cumulative neuronal activity into a single, stable fluorescence parameter and coupled it with fluorescence-activated cell sorting (FACS), establishing a high-throughput method for detecting neuronal activity at single-cell resolution (Figure 1A). We further integrated this activity-based sorting approach with a CRISPRi genetic

screening platform in human induced pluripotent stem cell (iPSC)-derived neurons (iNeurons)[27] , developing a pooled high-throughput screening method for neuronal activity. As a proof-of-principle, we applied our CaMPARI-CRISPRi platform to screen a group of DEGs identified via single-cell RNA sequencing (scRNA-seq) during long-term memory formation[13] . Our screen uncovered both known and previously uncharacterized modulators of neuronal activity. Notably, we identify *TMEM50A*, a gene of previously unknown function, as an essential factor for neuronal activity that acts by controlling multivesicular body (MVB) formation. Loss of *TMEM50A* reduces synapse density, disrupts neuronal electrophysiological properties, and alters behavior in mice, including deficits in remote memory.

RESULTS

Establishing a CaMPARI2-based high-throughput method to quantify neuronal activity in human iNeurons

The Ca^{2+}-dependent, irreversible photoconversion of CaMPARI converts transient neuronal activity into a stable fluorescence readout, quantified as the red-to-green (R/G) ratio. This enables cumulative neuronal activity to be measured post hoc in a high-throughput, scalable manner by flow cytometry: for a fixed illumination window, a higher CaMPARI R/G ratio indicates greater Ca^{2+} accumulation and therefore stronger neuronal activity (Figure 1A).

To enable pooled CRISPR screens of neuronal activity, we integrated CaMPARI into our previously developed CRISPRi screening platform in human iNeurons. We introduced CaMPARI2, an improved version

of CaMPARI, via lentiviral infection into iPSCs harboring doxycycline-inducible NGN2 cassette in the AAVS1 safe harbor locus and CRISPRi machinery (dCas9-BFP-KRAB) cassette in the CLYBL locus[28] (Figure 1B). Upon NGN2 induction, iPSCs rapidly differentiate into glutamatergic neurons[29] . These iNeurons are functional excitatory neurons that form excitatory synapses and exhibit robust spontaneous and evoked activity, with electrophysiological properties reaching a steady state at 4–6 weeks [30] .

Consistent with prior characterization, RNA-seq analysis of our iNeurons at different stages of differentiation (days 14, 21, 28, and 35) revealed marked upregulation of genes required for neuronal activity—including ion channels, glutamate receptors, vesicle release machinery, and synapse formation—after day 14, plateauing at days 21–28 (Figure 1C). Whole-cell patch-clamp recordings of spontaneous and current injection-evoked action potential firing further confirmed that day-28 iNeurons exhibit robust neuronal activity (Figure 1D). We therefore used day-28 iNeurons in subsequent experiments.

We next characterized whether CaMPARI2 can reliably detect neuronal activity in iNeurons. Using fluorescence microscopy, we observed robust photoconversion in CaMPARI2-iNeurons illuminated with violet light for 5 min (Figure 1E). Importantly, this photoconversion was readily quantified by flow cytometry, with the R/G intensity ratio increasing as a function of illumination time over the 0–10 min range. To ensure sufficient signal while minimizing

light-induced cytotoxicity, we used 5 min of illumination in subsequent experiments.

We then tested whether CaMPARI2 captures neuronal activity changes. Glutamate stimulation of iNeurons elicited a dose-dependent increase in CaMPARI2 photoconversion, demonstrating that CaMPARI2 reliably reports neuronal activity in response to excitatory input (Figure 1G). To determine whether CaMPARI2 can also detect genetically driven activity modulation, we performed CRISPRi knockdown of two established regulators of neuronal excitability and synaptic function: *TSC1*[31] , a key negative regulator of mTOR signaling implicated in epilepsy and neurodevelopmental disorders, and *STXBP1*[32] , which encodes a presynaptic vesicle release factor and is associated with developmental and epileptic encephalopathy[33] . Consistent with reports of decreased activity associated with loss of these genes, flow cytometry revealed reduced CaMPARI2 R/G ratios under both 1-min and 5-min illumination following knockdown of either *TSC1* or *STXBP1* in iNeurons (Figure 1H). Collectively, these data establish CaMPARI2 photoconversion as a robust, scalable, flow cytometry–compatible readout for quantifying neuronal activity in human iNeurons.

A CaMPARI2-based CRISPRi screen uncovers known and novel neuronal activity regulators

Next, we conducted a proof-of-principle CaMPARI2-based CRISPRi screen on neuronal activity in iNeurons. To maximize the chance of identifying key regulators, we constructed a biologically informed sgRNA library targeting a set of high-confidence remote-memory-

associated DEGs in excitatory neurons identified in a recent scRNA-seq study[13] . These memory-associated genes reflect stable, long-lasting transcriptional programs linked to remote memory storage and are enriched for pathways involved in synaptic function, neuronal excitability, and activity-dependent plasticity. The sgRNA library comprised 320 sgRNAs targeting 64 genes (5 sgRNAs per gene), alongside 28 non-targeting control sgRNAs (Figure 2A, Supplementary Data 1). The library was delivered into CaMPARI2-expressing CRISPRi-iPSCs via lentiviral infection, followed by selection, expansion, and differentiation. At Day 28, neurons were illuminated with violet light for 5 min to induce activity dependent CaMPARI2 photoconversion. Subsequently, neurons were sorted by FACS into populations with the highest 30% or lowest 30% R/G ratios. Next-generation sequencing (NGS) was then used to quantify sgRNA representation in each population, and hits were called using the MAGeCK-iNC pipeline[27,34] .

The screen uncovered both positive and negative hits, whose knockdown increased or decreased CaMPARI2 signal respectively (Figure 2B, Supplementary Data 2). Among the hits, we recovered multiple genes previously implicated in synaptic function, intrinsic excitability, or epilepsy[35] , including *ATP6V0C*[86] , *HNRNPH2*[87] , *NSF*[38] , *STX1B*[89] , *NCDN*[40] , *GSK3B*[41] , *PAK1*[42] , *SDHA*[43] , *VAMP2*[44] , *PIGQ*[45] , and *ALG2*[85] , validating the reliability of our screening strategy.

Interestingly, among the negative hits we identified *TMEM50A*, a putative transmembrane protein with previously uncharacterized

function (Figure 2B), and therefore prioritized it for follow-up. To confirm the *TMEM50A* phenotype and rule out potential sgRNA off-target effects, we individually cloned three independent sgRNAs targeting *TMEM50A*. Knockdown of *TMEM50A* with each of the three sgRNAs in iNeurons significantly reduced CaMPARI2 photoconversion compared to non-targeting controls (Figure 2C, S2A), thereby validating the screening result, and excluding off-target effects.

To determine whether the reduction in CaMPARI2 signal reflected bona fide changes in neuronal activity, we generated *TMEM50A* knockout (KO) iPSCs (Figure S2B–C) and assessed the electrophysiological properties of the derived iNeurons using whole-cell patch-clamp. Voltage-clamp recordings revealed a significant reduction in both sEPSC frequency and amplitude in *TMEM50A* KO iNeurons, indicating a marked impairment in synaptic transmission (Figure 2D-E). Additionally, current-clamp analysis showed that *TMEM50A* KO iNeurons exhibited a significant reduction in the number of action potentials generated in response to depolarizing current steps compared to controls (Figure 2F-G), indicating reduced intrinsic excitability. Together, these data demonstrate that TMEM50A is critical for maintaining neuronal activity levels by supporting both excitatory synaptic transmission and intrinsic neuronal responsiveness.

In summary, our CaMPARI2-based CRISPRi screen provides a robust approach for identifying neuronal activity regulators and identifies TMEM50A as a novel factor required to maintain normal neuronal

activity in human iNeurons.

TMEM50A localizes to multivesicular bodies

TMEM50A is predicted to encode a four-pass transmembrane protein (Figure S1A) and is highly conserved across vertebrates (Figure S1B). *TMEM50A* has a paralog in the human genome, TMEM50B; however, *TMEM50A* is the predominant paralog expressed in iNeurons, with consistently higher expression than *TMEM50B* across differentiation stages (Figure S1C).

To begin elucidating how TMEM50A regulates neuronal activity, we first determined its subcellular localization. Because of the lack of suitable antibodies, we initially examined its localization using a fluorescently tagged TMEM50A construct (TMEM50A–HA–GFP) in COS7 cells. However, we found that the expression level of exogenous TMEM50A profoundly affect its localization: transient overexpression produced prominent co-localization with the ER marker Sec61B[46], whereas lower-level expression via lentiviral transduction reduced the reticular ER signal and revealed a punctate, vesicle-like distribution (Figure S3A). Live-cell imaging further showed that these vesicles were motile and moved along the ER network (Movie S1).

To determine the localization of endogenous TMEM50A, we generated C-terminal 3×FLAG–mNeonGreen knock-in (KI) lines using CRISPR/Cas9-mediated homology-directed repair (HDR) in both HEK293T cells and iPSCs (Figure S3B). Using super-resolution

structured illumination microscopy (SIM), we observed predominantly vesicular localization of TMEM50A in both HEK293T KI cells and iNeurons derived from the iPSC KI line. In iNeurons, TMEM50A-positive vesicles were detected in both soma and neurites (Figure 3B–C; Movies S2–S4).

To define the identity of these vesicles, we performed co-localization analysis with markers of distinct membrane compartments[47], including mRuby-RAB1A (ERGIC), mRuby-RAB5A (early endosome), mRuby-RAB7A (late endosome), mRuby-RAB11A (recycling endosome), and LAMP1 (lysosome). TMEM50A showed predominant co-localization with endosomal markers but not lysosomes (Figure S3C–D).

We next performed interactome profiling by immunoprecipitation–mass spectrometry (IP–MS) using FLAG pull-down from TMEM50A–3×FLAG–mNeonGreen knock-in iNeurons, with IgG pull-down as a control (Figure 3D; Supplementary Data 3). Notably, many TMEM50A interactors are involved in vesicular trafficking, including AP2B1[48], AP2M1[49], AP2S1[50], AP2A2[48], RAB11B[47,51], TMEM87A[52], PIK3R4[53], and VPS51[54]. In addition, several ESCRT/MVB-related factors were identified, including CHMP7[55], CHMP1B[55], CHMP4B[55], VTA1[56], and HGS[57]. Gene Ontology analysis further highlighted enrichment for MVB-related pathways (Figure 3E). Consistent with these proteomic data, co-localization analysis with the MVB marker CD63 confirmed that TMEM50A is enriched on MVBs (Figure 3F).

TMEM50A forms a complex with LEPROTL1 and interacts with ESCRT-III to maintain MVB function

Among the TMEM50A interactors identified by IP–MS, LEPROTL1 emerged as a particularly interesting candidate. Although LEPROTL1 function in mammalian cells remains poorly characterized, its yeast homolog Vps55 has been reported to interact with Vps68, the yeast homolog of TMEM50A[58,59] . AlphaFold3-based structural modeling revealed that yeast Vps55, Vps68, and the Vps55–Vps68 complex closely resemble human LEPROTL1, TMEM50A, and the LEPROTL1–TMEM50A complex, respectively, with RMSD values of 1.03 Å, 3.44 Å, and 1.25 Å (Figure 4A).

To determine whether TMEM50A forms a similar complex with LEPROTL1 in mammalian cells, we performed co-immunoprecipitation (co-IP) experiments, which demonstrated a robust association between TMEM50A and LEPROTL1 (Figure 4B). Consistently, immunofluorescence analysis revealed strong co-localization of TMEM50A and LEPROTL1 (Figure 4C–D). Functionally, LEPROTL1 knockdown reduced neuronal activity to a similar extent as TMEM50A knockdown as measured by CaMPARI2, and simultaneous knockdown of both genes did not further enhance the phenotype relative to either single knockdown (Figure 4E; Figure 2C), indicating that TMEM50A and LEPROTL1 act in the same pathway as a functional complex.

Multiple ESCRT-III components, including CHMP1B, CHMP4B, and

CHMP7, were also identified as TMEM50A interactors (Figure 3B). Co-IP assays further confirmed interactions among TMEM50A, LEPROTL1, and CHMP4B (Figure 4F–G). Given the central role of ESCRT-III in MVB biogenesis, we asked whether the TMEM50A–LEPROTL1 complex localizes with ESCRT-III on MVBs. Using TMEM50A–mNeonGreen and LEPROTL1–mRuby double knock-in cells, we observed substantial co-localization of TMEM50A and LEPROTL1 with CHMP4B and the MVB marker CD63 (Figure 4H).

Based on these observations, we hypothesized that the TMEM50A–LEPROTL1 complex supports MVB function via ESCRT-III. To test this, we performed an EGFR degradation assay, in which ligand-stimulated EGFR is sorted into MVB intraluminal vesicles and subsequently delivered to lysosomes for degradation[60] (Figure 4I). Notably, *TMEM50A* knockout significantly delayed EGFR degradation compared to control cells (Figure 4J–K), indicating defective MVB-mediated cargo degradation.

To assess the specificity of this defect, we examined lysosomal integrity using LysoTracker and retrograde transport using cholera toxin B (CTxB) internalization. Neither assay revealed detectable differences between *TMEM50A* knockdown and control cells (Figure S4A–D).

ESCRT complexes drive intraluminal vesicle formation during MVB biogenesis through membrane remodeling and scission[61–63] . To determine the impact of TMEM50A on MVB ultrastructure in vivo,

we performed scanning electron microscopy (SEM) on anterior cingulate cortex (ACC) sections from *Tmem50a*-KO mice. Ultrastructural analysis revealed a marked reduction in the number of ILVs within MVBs in *Tmem50a*-KO mice compared with WT controls (Figure 4L–M). This phenotype is consistent with defects observed upon ESCRT loss[64] , further supporting a role for TMEM50A in ESCRT-dependent intraluminal vesicle formation during MVB biogenesis.

In summary, TMEM50A forms a complex with LEPROTL1 that associates with ESCRT-III at MVBs and is required for efficient ESCRT-dependent intraluminal vesicle formation and MVB-mediated cargo degradation.

TMEM50A **loss remodels neuron surface proteome and reduces synapse density**

Because MVBs play a central role in plasma membrane protein turnover[65,66] , we performed cell-surface biotinylation and affinity purification in WT and *TMEM50A* KO iNeurons, followed by quantitative proteomics to measure changes in surface protein abundance (Figure 5A). *TMEM50A* KO neurons showed widespread alterations in the abundance of plasma membrane proteins (Figure 5B, Supplementary Data 4). Gene ontology analysis of the altered surface proteome revealed enrichment for pathways related to cell–cell adhesion, axon guidance, and synapse organization (Figure 5C). Given the synaptic transmission defects observed in *TMEM50A* KO iNeurons (Figure 2), we next asked whether synapse organization is impaired. Immunostaining for the presynaptic marker Synapsin1/2,

the postsynaptic marker PSD95 and the dendritc marker MAP2 revealed a significant reduction in synaptic density in *TMEM50A* KO iNeurons. In contrast, puncta size, dendrite number, and soma size showed no significant changes (Figure 5D–E, S5A).

We also used mouse primary neurons to validate these findings. We isolated primary cortical neurons from CRISPRi transgenic mice expressing the dCas9–KRAB machinery and infected them with either a control sgRNA or a *Tmem50a*-targeting sgRNA via AAV (Figure 6A). RT–qPCR confirmed a strong reduction of *Tmem50a* mRNA in neurons transduced with the *Tmem50a* sgRNA (Figure 6B). Immunofluorescence analysis revealed synaptic phenotypes consistent with those observed in human iNeurons, showing a significant reduction in synaptic density, while puncta size, dendrite number, and soma size remained unchanged (Figure 6C–D, S5B).

To assess synaptic alterations *in vivo*, we analyzed synaptic ultrastructure from the SEM images of ACC sections from *Tmem50a*-KO mice. We quantified synaptic cleft width, the number of synaptic vesicles (SVs) per bouton, and postsynaptic density (PSD) length at both inhibitory and excitatory synapses. None of these ultrastructural parameters differed significantly between *Tmem50a*-KO and WT mice (Figure 6E–F). In contrast, synapse density was significantly reduced in *Tmem50a* -KO mice (Figure 6E–F), consistent with the reduced synaptic puncta observed in cultured neurons.

In summary, TMEM50A loss causes broad remodeling of the neuronal surface proteome and leads to a reduction in synapse density.

Tmem50a **loss alters memory- and anxiety-related behaviors in mice**

Since *TMEM50A* is among a remote fear memory associated gene program, we then assessed its effect on contextual fear memory using a standard fear-conditioning paradigm (Figure 7A). *Tmem50a*-KO mice exhibited freezing behavior comparable to WT controls during recent memory retrieval (Day 5), indicating intact recent memory (Figure 7B). In contrast, during remote memory retrieval (Day 21), *Tmem50a*-KO mice displayed significantly reduced freezing compared with WT mice, indicative of impaired remote memory consolidation (Figure 7B).

We next performed the open field test (Figure 7C). *Tmem50a*-KO mice spent significantly more time in the center of the arena than WT mice, suggesting reduced anxiety-like behavior. Total distance traveled did not differ between *Tmem50a*-KO and WT mice, indicating that this effect was not attributable to altered general locomotor activity.

Finally, we assessed motor coordination using the rotarod test (Figure 7D). *Tmem50a*-KO and WT mice showed no differences in latency to fall or speed at the time of fall, indicating that *Tmem50a* loss does not impair motor coordination or balance.

DISCUSSION

Transcriptomic and genomic studies have generated extensive catalogs of genes associated with brain activity and behavior in health and disease[10,17,67] . Yet functional characterization of these candidates has lagged far behind discovery. Here, we begin to address this gap by developing a high-throughput functional genomics platform that couples the calcium-integrating sensor CaMPARI2 with pooled CRISPRi screening in human iPSC-derived neurons. By converting cumulative neuronal activity into a stable, flow cytometry–readable signal, this system enables fluorescence-based sorting of large neuronal populations by activity state, thereby supporting unbiased pooled genetic screens to identify regulators of neuronal activity at scale.

Compared with patch-clamp electrophysiology and voltage or calcium imaging for detecting neuronal activity, CaMPARI offers a distinct advantage as a calcium recorder: activity is integrated over time and captured as a stable signal that can be measured after stimulation without continuous imaging. While CaMPARI was originally developed to label active neuronal ensembles in vivo, we demonstrate that it can quantitatively detect changes in neuronal activity induced by chemical stimulation or genetic perturbations when coupled with flow cytometry.

CRISPR-based functional genomics has emerged as a powerful approach for systematically interrogating gene function and has

been established in neuronal models. Most existing screens in neurons have focused on relatively simple phenotypes, such as cell survival. In this study, we extend CRISPR screening to a complex, neuron-specific phenotype—neuronal activity—thereby broadening the scope of CRISPR-based functional genomics in neuronal systems.

As a proof of principle, we screened a focused library of memory-associated DEGs. The screen recovered established regulators of synaptic function and excitability—including *NCDN*[40] , *STX1B*[68] , and *GSK3B*[41] . The screen also uncovered previously uncharacterized candidates, among which we selected *TMEM50A* for further validation and characterization. *TMEM50A* encodes a predicted four-pass transmembrane protein of unknown function in mammalian cells. Its yeast ortholog, Vps68, interacts with Vps55 (the yeast homolog of LEPROTL1) and with ESCRT-III components, and has been implicated in vacuolar protein sorting[58,69] . Our data indicate that these interactions are conserved in mammalian cells: using IP-MS, co-immunoprecipitation, and super-resolution imaging, we demonstrate that TMEM50A forms a complex with LEPROTL1 that localizes to MVBs and associates with the ESCRT-III component CHMP4B. Functionally, TMEM50A is required for efficient intraluminal vesicle formation and MVB-mediated cargo degradation.

The ESCRT/MVB pathway is central to plasma membrane protein turnover and has been increasingly implicated in neurological disease, including neurodegeneration and synaptopathies[70–72] . Consistent with these roles, we show that TMEM50A loss broadly

remodels the neuronal surface proteome, reduces synapse density, diminishes synaptic transmission and intrinsic excitability, and leads to behavioral phenotypes including impaired remote memory and altered anxiety-like behavior.

Limitations and future directions

First, our proof-of-principal screen used a small, focused library. Given the scalability of our platform, it can be readily extended to larger, even genome-wide, libraries in future studies to achieve a more systematic and comprehensive identification of genes regulating neuronal activity across diverse contexts. Indeed, while this manuscript was in preparation, a study utilizing a conceptually similar strategy reported screens for regulators of neuronal excitability under glutamate-evoked conditions, highlighting the broad applicability of pooled activity screening[73] .

Second, our screen was performed in NGN2-induced human iNeurons in 2D culture. Extending this system to more complex models—such as brain organoids, assembloids, or in vivo settings—will enable screening in more physiologically relevant contexts. Furthermore, applying this platform to disease contexts, such as patient-derived iNeurons, could enable identification of genetic modifiers that rescue pathological neuronal activity, leading to the discovery of potential therapeutic targets.

Third, while we demonstrate that TMEM50A interacts with LEPROTL1 and CHMP4B to regulate MVB function, the precise

molecular mechanism remains to be defined. Future structural analysis and biochemical reconstitution studies will be valuable for elucidating how the TMEM50A–LEPROTL1 complex physically engages ESCRT-III machinery to facilitate membrane remodeling and intraluminal vesicle biogenesis.

MATERIALS AND METHODS

Cell Culture

Cell lines

HEK293T and COS-7 cells (ATCC) were cultured in DMEM (Gibco, C11995500BT) supplemented with 10% FBS (TransGen Biotech, FS301-02) and 1% penicillin–streptomycin (Aladdin, P301861) at 37 °C in a humidified incubator with 5% CO_2. Cells were passaged every 2–3 d at a 1:4–1:8 split ratio using 0.05% trypsin–EDTA (Yeasen, 40127ES60).

hiPSC culture and iNeuron differentiation

hiPSCs harboring dCas9-BFP-KRAB and tet-on NGN2 (WTc11 background; Coriell GM29371) were maintained in StemFlex medium (Thermo Fisher Scientific, A3349401) on growth factor–reduced, phenol red–free, LDEV-free Matrigel (Corning, 356231) diluted 1:200 in DPBS (Invitrogen, C14190500BT). Cultures were maintained at 37 °C with 5% CO_2 and fed the day after seeding and every other day thereafter. For passaging at ~80% confluence, cells were rinsed with DPBS, incubated with Accutase (STEMCELL Technologies, 07922) for 3–5 min at 37 °C, diluted 3–5× with DPBS, gently triturated to single cells, and centrifuged at 200 × g for 5 min at room temperature. Pellets were resuspended in StemFlex supplemented with Y-27632 ROCK inhibitor (Selleck, S1049), counted, and replated onto fresh Matrigel-coated dishes at a 1:6–1:10 split ratio. ROCK inhibitor was maintained for the first 24 h post-passaging and then removed.

iNeurons were generated as previously described[27] . Briefly, hiPSCs were pre-differentiated on Matrigel-coated plates in N2 pre-differentiation medium consisting of KnockOut DMEM/F12, 1× MEM non-essential amino acids, 1× N2 Supplement (Gibco, 17502-048), NT-3 (10 ng/mL; PeproTech, 450-03), BDNF (10 ng/mL; PeproTech, 450-02), mouse laminin (1 μg/mL; Thermo Fisher Scientific, 23017-015), ROCK inhibitor (10 nM), and doxycycline (2 μg/mL) to induce mNGN2 expression. After 3 d, cells were replated (designated Day 0) onto plates coated with 0.1% PEI and laminin in neuronal medium containing a 1:1 mixture of DMEM/F12 (Gibco, 11320-033) and Neurobasal-A (Gibco, 10888-022), 1× MEM non-essential amino acids, 0.5× GlutaMAX (Gibco, 35050-061), 0.5× N2 Supplement, 0.5× B27 Supplement (Gibco, 17504-044), NT-3 (10 ng/mL), and BDNF (10 ng/mL). Half medium was replaced weekly.

Primary mouse neuron culture

Primary cortical neurons were prepared from embryonic mice (E14–E18) as previously described with minor modifications[74] . Cortices were dissociated with 0.25% trypsin–EDTA (Gibco, 25200072) for 10 min at 37 °C, followed by trituration using a Pasteur pipette. Digestion was terminated with DMEM/F12 (Gibco, C11330500BT) supplemented with 10% FBS (Gibco, A5669701), and DNase I was added to reduce aggregation. Dissociated neurons were plated onto poly-D-lysine–coated glass coverslips (Beyotime, ST508) in 24-well plates and maintained in Neurobasal medium (Thermo Fisher Scientific, 10888022) supplemented with 2% B27 (Gibco, 17504044) and 0.5% GlutaMAX (Gibco, 35050061) at 37 °C with 5% CO_2.

Mycoplasma testing

Mycoplasma contamination was routinely screened by PCR, and all cultures were confirmed mycoplasma-free.

Mice

Tmem50a-KO mice (C57BL/6JCya-Tmem50aem1) were purchased from Cyagen. This line carries a conventional *Tmem50a* knockout allele generated by CRISPR/Cas9-mediated deletion (NCBI Gene ID: 71817). Two guide RNAs targeting exon regions were used: CTTAAGAATCATATGTCAGA and AAAATTCCCAGCCCTTGGGT. CRISPRi mice ($H11^{dCas9\text{-}KRAB}$) were purchased from The Jackson Laboratory (#030000). These mice express a catalytically inactive Cas9 fused to the KRAB repressor, inserted into the H11 locus of the mouse genome by targeted knock-in. C57BL/6 wild-type mice were obtained from Guangdong Medical Laboratory Animal Center. All mice were group-housed (maximum 5 per cage) in a specific-pathogen-free (SPF) environment. They were maintained on a 12 h light–dark cycle (lights on 08:00–20:00) with ad libitum access to food and water. Male mice aged 6–8 weeks were used for all experiments. All surgical procedures were performed under isoflurane or tribromoethanol anesthesia, and every effort was made to minimize pain and distress. All animal experimental procedures were approved by the Animal Care and Use Committee at Shenzhen Bay Laboratory (AEJX20220201A) and Shenzhen Medical Academy of Research and Translation (SMART-IACUC-2025-A023) and conducted in accordance with institutional guidelines.

Lentiviral production

HEK293T cells were seeded the day prior at ~30% density and allowed to reach ~70–80% confluence on the day of transfection. For small-scale lentiviral packaging in 6-well plates, 1 μg transfer plasmid and 1 μg third-generation packaging mix were diluted in 200 μL Opti-MEM and combined with 6 μg PEI (Yeasen, 40816ES01) for each well. For large-scale packaging of sgRNA library, one 15-cm dish was used with 15 μg packaging plasmid and 15 μg library plasmid diluted in 2 mL Opti-MEM with 90 μg PEI. The transfection mixture was incubated at room temperature for 15 min and then added to the cells. At 48 h post-transfection, supernatants were collected, passed through a 0.45 μm PVDF syringe filter into conical tubes, mixed with ¼ volume lentiviral pellet solution, and held at 4 °C for 24 h. Virus-containing supernatants were centrifuged at 3,500 × g for 30 min at 4 °C, the supernatant was aspirated, and a brief clarification spin (3,500 × g, 2 min, 4 °C) was performed. Pellets were resuspended in DPBS, aliquoted, and stored at −80 °C.

AAV production and transduction of primary neuron

Recombinant adeno-associated viruses (AAVs) were packaged at a titer of 1×10^{12} by Institute of Molecular Physiology, Shenzhen Bay Laboratory. Primary cortical neurons were transduced at day in vitro 4 (DIV4), with control and experimental viruses applied at comparable titers.

CaMPARI2 photoconversion assay

The CaMPARI2 cassette (Addgene #101060) was subcloned into a lentiviral vector containing a CAG promoter and an upstream UCOE element via Gibson assembly. A stable CaMPARI2 hiPSC line was

generated by lentiviral transduction of hiPSCs harboring dCas9-BFP-KRAB and tet-on NGN2.

Photoconversion was induced by 405-nm LED illumination of Day 28 CaMPARI2 iNeurons and quantified by confocal microscopy (Nikon ECLIPSE Ts2) or flow cytometry (BD FACSAria SORP). For flow cytometry, cells were enzymatically dissociated with papain (Worthington, PAP2; 20 U/mL in 1× DPBS) supplemented with DNase I (10 U/mL) for 15 min at 37 °C. Digestion was quenched with 3 volumes of DMEM containing 10% FBS, and cells were pelleted (500 × g, 10 min). Pellets were resuspended in DPBS with 5% FBS and analyzed by flow cytometry; data were processed using FlowJo v10.

Generation of sgRNA library targeting memory-associated genes

A set of memory-associated genes was derived from a published scRNA-seq study that identified 64 remote-memory–associated DEGs in excitatory neurons[13] . For each gene, the top five sgRNAs were selected from the CRISPRi-v2 library (ref), and 28 non-targeting control sgRNAs were included, yielding a final library of 348 sgRNAs (Supplementary Data 1). An sgRNA oligonucleotide pool was synthesized (GENEWIZ) and cloned into pCRISPRia-v2 (Addgene #84832) using the BstXI and BlpI restriction sites. To assess library quality, the sgRNA-containing region was PCR-amplified using Phanta Flash Master Mix (Vazyme, P520) according to the manufacturer’s instructions, and PCR products were analyzed by next-generation sequencing.

CaMPARI2-based CRISPRi screening

sgRNA library was transduced into hiPSCs via lentiviral infection at a multiplicity of infection (MOI) of ~0.3, followed by puromycin selection. After expansion, hiPSCs were differentiated into iNeurons and plated at 1×10^{7} cells per plate onto 10-cm PEI-coated dishes.

On Day 28, iNeurons were subjected to CaMPARI2 photoconversion followed by papain dissociation. Dissociated neurons were transferred to 15-mL conical tubes and centrifuged at 500 × g for 5 min. Pellets were gently resuspended in 2 mL DPBS, passed through a 100-µm cell strainer to remove axonal debris and incompletely dissociated aggregates, and the filtrate was transferred to flow cytometry tubes for FACS.

For FACS, cells were first gated by forward and side scatter to select live singlets, then sorted based on the CaMPARI2 red-to-green fluorescence ratio (R/G; green excited at 488 nm and collected at ~530/30 nm, red excited at 561 nm and collected at ~610/20 nm). The top 30% (“high-ratio”) and bottom 30% (“low-ratio”) fractions were collected. Sorted cells were pelleted at 500 × g for 5 min, and genomic DNA was extracted using the TIANamp Genomic DNA Kit (Tiangen, DP304-03) according to the manufacturer’s instructions. sgRNA cassettes were PCR-amplified with adapter primers using Phanta Flash Master Mix (Vazyme, P520) to generate sequencing-ready products. PCR products were purified with Hieff NGS® DNA

Selection Beads V2 (YEASEN, 12418ES08) and subjected to next-generation sequencing.

The MAGeCK-iNC pipeline was used to evaluate sgRNA- and gene-level phenotypes relative to non-targeting controls[34]. Raw sequencing reads were trimmed and aligned using publicly available custom scripts from the Kampmann Lab (https://kampmannlab.ucsf.edu/resources). Phenotype scores and p-values for target genes and non-targeting controls were computed using the Mann–Whitney U test. Hit genes were defined using an empirical false discovery rate (FDR) threshold of 0.01 (Supplementary Data 2).

sgRNA cloning

Individual sgRNAs were synthesized and cloned into the pLG15 vector using the BstXI and Bpu1102I restriction sites as previously described[27]. The pLG15 vector contains a mouse U6 promoter driving sgRNA expression, and an EF1α promoter that drives puromycin resistance cassette and BFP for selection. Constructs were verified by Sanger sequencing. Individual sgRNAs used in this study are listed in Supplementary Data 5.

RNA extraction and quantitative real-time PCR

Total RNA was isolated with the MolPure® Cell RNA Kit (Yeasen, 19231ES50) following the manufacturer's instructions. Reverse transcription was carried out using the HiScript III 1st Strand cDNA Synthesis Kit (Vazyme, R312). Quantitative real-time PCR was

performed on an FDQ-96A real-time fluorescence detection system using AceQ qPCR SYBR Green Master Mix (Vazyme, CQ111-02) according to the supplier's protocol. GAPDH served as the endogenous normalization control. Primers used in this study are listed in Supplementary Data 5.

CRISPR-mediated gene knockout

sgRNAs targeting TMEM50A exon 1 were designed using CHOPCHOP[75] and cloned into pX459 (Addgene #62988). Constructs were verified by Sanger sequencing. hiPSCs were transfected using Lipofectamine™ Stem (Invitrogen, STEM00003); HEK293T cells were transfected with PEI (Yeasen, 40816ES01). At 48 h post-transfection, cells were selected with puromycin, recovered for 48 h, and genotyped. Editing efficiency was assessed by ICE (Synthego). For clonal isolation, 250 cells were seeded on Matrigel-coated 35-mm dishes; colonies were manually picked into 48-well plates for expansion and genotyping.

CRISPR-mediated endogenous knock-in

An sgRNA targeting the desired knock-in site was cloned into pX459 (Addgene #62988). A dsDNA donor containing microhomology arms flanking the cut site, a 3×FLAG tag, and a fluorescent protein cassette was co-transfected using Hieff Trans (Yeasen, 40802ES02) for HEK293T cells or Lipofectamine™ Stem (Invitrogen, STEM00003) for hiPSCs. Puromycin (2 μg/mL) was applied 48 h post-transfection for 72 h, followed by recovery. Fluorescent-positive cells were single-cell sorted (BD FACSAria SORP) into 96-well plates

(one cell per well). After ~2 weeks, clones were genotyped by PCR and validated by Sanger sequencing.

Electrophysiology

EPSC recording was performed as described previously [76,77]. Electrodes had a resistance of 4-5 MΩ when filled with the pipette solution, which contained: 140 mM KCl, 0.5 mM EGTA, 5 mM HEPES and 3 mM Mg-ATP (pH 7.4 with KOH). The extracellular solution contained: 140 mM NaCl, 3 mM KCl, 2 mM $MgCl_2$, 2 mM $CaCl_2$, 10 mM HEPES (pH 7.4 with NaOH). The whole-cell recording configuration was obtained in voltage clamp mode with an EPC-10 amplifier (HEKA) at a sampling rate of 20 kHz. For action potential (AP) recording, APs were evoked by a set of stepped increasing currents (-20 to 120 pA, 300 ms; in increments of 10 pA).

Immunoprecipitation-Mass Spectrometry (IP-MS)

TMEM50A knock-in iNeurons were cultured on twelve 15-cm dishes (3×10^7 cells/dish). On Day 21, neurons were washed twice with ice-cold DPBS and scraped into DPBS. Cells were resuspended in 2 mL lysis buffer and lysed on ice for 30 min with occasional vortexing. Lysates were clarified at 14,000 rpm for 10 min at 4 °C.

To 1 mL clarified lysate, 80 µL BeyoMag Anti-FLAG beads (Beyotime, P2115) and 80 µL BeyoMag Mouse IgG beads (Beyotime, P2171) were added and rotated overnight at 4 °C. Beads were collected, washed twice with TBST (TBS + 0.1% Tween-20), and bound proteins were eluted and analyzed by SDS–PAGE followed by MS to identify TMEM50A interactors (Supplementary Data 3).

Western blot

Cells were collected and washed with cold DPBS. Cells were lysed with lysis buffer (1% DDM, 150 mM HEPES, [pH 7.4], 150 mM NaCl) supplemented with EDTA-free protease inhibitor cocktail (Epizyme, GRF101) on ice for 30 min. The soluble fractions of cell lysates were isolated by centrifugation at 15,000 rpm for 10 min at 4 °C. Proteins were denatured by the addition of 5 × SDS sampling buffer and no boiling. Samples were subjected to SDS-PAGE and immunoblotting analysis.

Co-immunoprecipitation (Co-IP)

HEK293T cells were plated on a 10 cm dish for 24 h before transfection with pcDNA3.1-GFP, pcDNA3.1-TMEM50A-GFP, pcDNA3.1-LEPROTL1-myc-mRuby, or pcDNA3.1-CHMP4B-V5-BFP. After 48 h, cells were lysed in lysis buffer, and the lysates were centrifuged at 15,000 rpm for 10 minutes at 4°C. The supernatant was incubated with ABM® Anti-GFP VHH Agarose (ABMagic, MA108) or ABM® Anti-MYC VHH Magarose (ABMagic, MA105) at 4°C overnight. After washing, the beads were denatured and analyzed by immunoblotting.

EGFR degradation assay

HEK293T cells were seeded at 0.5×10^6 cells per well into five wells of a 12-well plate and incubated for 24 h at 37 °C, 5% CO_2. The medium was then replaced with serum- and antibiotic-free DMEM, and cells were serum-starved overnight. Cells were washed twice

with DPBS, then 0.5mL of EGF-containing DMEM (200 ng/ml) was added per well. Plates were incubated at 37 °C, 5% CO_2 for 0, 20, 40, 80, and 120 min. At each time point, medium was aspirated, and cells were detached with trypsin, collected, and centrifuged at 200 × g for 5 min. Pellets were washed three times with DPBS and the final pellet was used for lysis. Cells were lysed on ice for 30 min in 100 µL lysis buffer (1% NP-40, 200 mM NaCl, 50 mM Tris-HCl, pH 8.0; optionally supplemented with protease/phosphatase inhibitors). Lysates were clarified, resolved by SDS–PAGE, and analyzed by immunoblotting with antibodies against EGFR (Cell Signaling Technology, 4267S) and GAPDH (Proteintech, HRP-60004).

Surface Biotinylation Assay

Cell surface biotinylation was performed using the Pierce™ Cell Surface Protein Biotinylation Kit according to the manufacturer's instructions. WT and *TMEM50A* KO iNeurons were rinsed with DPBS and incubated with 0.125 mg/mL EZ-Link™ Sulfo-NHS-SS-Biotin (membrane-impermeable) in DPBS for 1 h at room temperature. The reaction was quenched with 50 mM glycine for 10 min. Cells were washed three times with ice-cold PBS, harvested, and lysed in 1 mL lysis buffer supplemented with a complete protease inhibitor cocktail. Lysates were clarified by centrifugation at 15,000 × g for 10 min at 4 °C, and protein concentrations were determined by BCA assay. A total of 500 µg protein was incubated with 60 µL NeutrAvidin agarose resin (Thermo Scientific) overnight at 4 °C with gentle agitation. Resin was washed three times with TBST, and biotinylated proteins were eluted using the kit elution buffer.

Cholera toxin subunit B (CTxB) assay

CTxB trafficking assay was performed as described previously[78] . HEK293T cells were incubated with cholera toxin subunit B (CTxB; 1:1000 in culture medium) for 5 min at 37 °C. Coverslips were washed and chased for 1 h, then cells were washed with PBS and fixed with 4% paraformaldehyde (PFA) for 10 min. Cells were immunostained for the Golgi marker GM130. Retrograde transport of CTxB was quantified by calculating the Pearson's colocalization coefficient between CTxB and GM130 in Fiji (ImageJ, NIH).

Immunocytochemistry

The immunocytochemistry experiments were conducted as previously described[79] . Briefly, cultured neurons on DIV14 were fixed with 4% paraformaldehyde (leagene #DF0135), permeabilised with 0.3% Triton X-100(Solarbio #T8200) for 20 minutes and blocked with 5% BSA (Solarbio #A8010) for 30 minutes. Cells were incubated with primary antibodies at 4 °C overnight, followed by incubation with fluorophore-conjugated secondary antibodies at room temperature for 2 hours, and coverslips were mounted using Fluoromount-G (Southern Biotech #0100-01). Images were acquired using a Zeiss LSM900 confocal microscope using identical acquisition settings across conditions. Z-stacks were collected at 0.5 mm intervals and maximum-intensity projections were used for quantification. The subsequent primary antibodies were used: Guinea pig anti-MAP2 (1:1000 dilution, SYSY #SYS-188-004), Rabbit anti-MAP2 (1:1000 dilution; SYSY; Cat# 188 002), Chicken anti-synapsin 1/2 (1:500 dilution, SYSY #106006), Mouse anti-PSD95 (1:500 dilution, Thermo MA1-046). Secondary antibodies included Goat anti-guinea pig IgG Alexa Fluor™ 647 (Invitrogen#A-21450),

Goat anti-mouse IgG Alexa Fluor™ 488 (Abcam #ab150113), Goat anti-Chicken IgY Alexa Fluor™ 488 (Thermo #A32931).Goat anti-rabbit IgG Alexa Fluor 647 (1:500 dilution; Sangon; Cat# D110078), Goat anti-mouse IgG Alexa Fluor 555 (1:1000 dilution; Thermo; Cat# A-21428), Goat anti-chicken IgG Alexa Fluor 488 (1:500 dilution; Sangon; Cat# D110061).

Scanning electron microscopy (SEM)

6-week-old C57BL/6 wild-type (n = 3) and TMEM50A-KO mice (n = 3) were used for SEM analysis. Mice were transcardially perfused first with ice-cold phosphate-buffered saline (PBS), followed by ice-cold fixative consisting of 4% paraformaldehyde and 1% glutaraldehyde in 0.1 M phosphate buffer (pH 7.2–7.4). The anterior cingulate cortex (ACC) was dissected using a brain matrix (RWD #68713) and cut into approximately 1 × 1 × 1 mm^3 blocks. Tissue samples were further fixed in 2.5% glutaraldehyde at room temperature for 2 h and then overnight at 4 °C. Subsequent sample processing was performed by the Bioimaging Core Facility of Shenzhen Bay Laboratory according to standard protocols. Images were acquired using a Zeiss Gemini 1 360 scanning electron microscope. SEM images were acquired at an accelerating voltage of 3.0 kV with a working distance of approximately 5.3 mm using a backscattered electron detector (Volume BSD), at a magnification of 10,000× and a resolution of 4,096 × 3,072 pixels.

Animal behavior

Contextual fear conditioning

Contextual fear conditioning was performed as previously described [13]. Mice were handled for 3 min per day for three consecutive days prior to training. On each experimental day, mice were transferred to the behavioral testing room and allowed to acclimate for at least 30 min before the session. Training was conducted in a fear-conditioning chamber (25 × 25 × 25 cm) equipped with a stainless-steel grid floor (Panlab, Harvard Apparatus) and maintained at 23–25 °C. All sessions were performed during the dark phase of the light/dark cycle and controlled using FREEZING and STARTLE software (Panlab, Harvard Apparatus). During encoding training, mice were allowed to freely explore the context for 3 min, followed by delivery of three-foot shocks (0.5 mA, 2 s) through the grid floor at 180 s, 242 s, and 304 s. Each shock was followed by a 60 s post-shock interval. Mice were removed from the chamber 60 s after the final shock and returned to their home cages. Chambers were thoroughly cleaned by 75% ethanol between animals. For retrieval testing, mice were re-exposed to the same context without shock for a 3-min session either 1 day (recent retrieval) or 16 days (remote retrieval) after training. Freezing behaviour was quantified automatically using the software, defined as immobility below a threshold of 4 arbitrary units (AU) for a minimum duration of 500 ms. The percentage of freezing was calculated over the entire 3-min test session.

Open field test

Open field test was conducted as previously described [80] . Mice were transferred to the behavioral testing room and allowed to acclimate for at least 30 min before the test. Mice were then individually placed in the center of an open field arena (RWD #63008, gray acrylic, 400

× 400 × 400 mm) and allowed to explore for 10 min. Total distance and time in central zone was automatically recorded by the SMARTPREMIUM Panlab Explore system (v3.0). The central zone was defined as a 16 × 16 cm area. Tests were performed under dim conditions (lights off) and maintained at 23–25 °C during the dark phase of the light/dark cycle, and the arena was thoroughly cleaned by 75% ethanol between trials.

Rotarod test

Rotarod tests were performed similarly as previously described [81] . Mice were transferred to the behavioral testing room and allowed to acclimate for at least 30 min before the session. Mice were first trained on the rotating rod at 5 rpm for 3 trials with 10 minutes intervals. Mice were first trained on a rotarod apparatus (Panlab Harvard Apparatus #LE8505, rod length 60 mm) at a constant speed of 5 rpm for three trials, with 10-min inter-trial intervals. Testing was then performed with an initial speed of 4 rpm that accelerated linearly to 40 rpm over 300 s. Each mouse underwent three test trials with 1-h inter-trial intervals, and the time latency to fall and the speed at the time to fall were automatically recorded by the system and the mean was used for analysis. The rod was cleaned thoroughly cleaned by 75% ethanol between animals.

QUANTIFICATION AND STATISTICAL ANALYSIS

All data were analyzed using GraphPad Prism 10 (GraphPad Software Inc.). Statistical comparisons between two groups were performed using Student’s t test, and comparisons involving three or more groups were performed using one-way or two-way ANOVA with

appropriate corrections for multiple comparisons. p values < 0.05, 0.01, and 0.001 were considered statistically significant and are denoted by *, **, and ***, respectively. Sample sizes and statistical methods for each quantification are provided in the figure legends.

Reference

1. Peters, H.C., Hu, H., Pongs, O., Storm, J.F., and Isbrandt, D. (2005). Conditional transgenic suppression of M channels in mouse brain reveals functions in neuronal excitability, resonance and behavior. Nat. Neurosci. *8*, 51–60. https://doi.org/10.1038/nn1375.

2. Andersen, O.M., Monti, G., Jensen, A.M.G., Waal, M.W.J. de, Hulsman, M., Olsen, J.G., and Holstege, H. (2024). Basic Science and Pathogenesis. Alzheimer's Dement. : J. Alzheimer's Assoc. *20 Suppl 1*, e084835. https://doi.org/10.1002/alz.084835.

3. Le, S., Menacho, C., and Prigione, A. (2024). Balancing neuronal activity to fight neurodevelopmental disorders. Trends Neurosci. *47*, 241–242. https://doi.org/10.1016/j.tins.2024.03.002.

4. Smith, R.S., and Walsh, C.A. (2020). Ion Channel Functions in Early Brain Development. Trends Neurosci. *43*, 103–114. https://doi.org/10.1016/j.tins.2019.12.004.

5. Sun, A.X., Yuan, Q., Fukuda, M., Yu, W., Yan, H., Lim, G.G.Y., Nai, M.H., D'Agostino, G.A., Tran, H.-D., Itahana, Y., et al. (2019). Potassium channel dysfunction in human neuronal models of Angelman syndrome. Science *366*, 1486–1492. https://doi.org/10.1126/science.aav5386.

6. Tyagi, S., Higerd-Rusli, G.P., Akin, E.J., Waxman, S.G., and Dib-Hajj, S.D. (2025). Sculpting excitable membranes: voltage-gated ion channel delivery and distribution. Nat. Rev. Neurosci. *26*, 313–332. https://doi.org/10.1038/s41583-025-00917-2.

7. Shah, M.M., Hammond, R.S., and Hoffman, D.A. (2010). Dendritic ion channel trafficking and plasticity. Trends Neurosci. *33*, 307–316. https://doi.org/10.1016/j.tins.2010.03.002.

8. Imbrici, P., Jaffe, S.L., Eunson, L.H., Davies, N.P., Herd, C., Robertson, R., Kullmann, D.M., and Hanna, M.G. (2004). Dysfunction of the brain calcium channel CaV2.1 in absence epilepsy and episodic ataxia. Brain *127*, 2682–2692. https://doi.org/10.1093/brain/awh301.

9. Aarts, M., Liu, Y., Liu, L., Besshoh, S., Arundine, M., Gurd, J.W., Wang, Y.-T., Salter, M.W., and Tymianski, M. (2002). Treatment of Ischemic Brain Damage by Perturbing NMDA Receptor- PSD-95 Protein Interactions. Science *298*, 846–850. https://doi.org/10.1126/science.1072873.

10. Yap, E.-L., and Greenberg, M.E. (2018). Activity-Regulated Transcription: Bridging the Gap between Neural Activity and Behavior. Neuron *100*, 330–348. https://doi.org/10.1016/j.neuron.2018.10.013.

11. Das, S., Lituma, P.J., Castillo, P.E., and Singer, R.H. (2023). Maintenance of a short-lived protein required for long-term memory involves cycles of transcription and local translation. Neuron *111*, 2051-2064.e6. https://doi.org/10.1016/j.neuron.2023.04.005.

12. Sun, W., Liu, Z., Jiang, X., Chen, M.B., Dong, H., Liu, J., Südhof, T.C., and Quake, S.R. (2024). Spatial transcriptomics reveal neuron–astrocyte synergy in long-term memory. Nature *627*, 374–381. https://doi.org/10.1038/s41586-023-07011-6.

13. Chen, M.B., Jiang, X., Quake, S.R., and Südhof, T.C. (2020). Persistent transcriptional programmes are associated with remote memory. Nature *587*, 437–442. https://doi.org/10.1038/s41586-020-2905-5.

14. Bahl, E., Chatterjee, S., Mukherjee, U., Elsadany, M., Vanrobaeys, Y., Lin, L.-C., McDonough, M., Resch, J., Giese, K.P., Abel, T., et al. (2024). Using deep learning to quantify neuronal activation from single-cell and spatial transcriptomic data. Nat. Commun. *15*, 779. https://doi.org/10.1038/s41467-023-44503-5.

15. Yamashita, K., Kinoshita, F.L., Yoshida, S.Y., Matsumoto, K., Mitani, T.T., Fujishima, H., Minami, Y., Morii, E., Yamada, R.G., Okada, S., et al. (2025). A whole-brain single-cell atlas of circadian neural activity in mice. Science, eaea3381. https://doi.org/10.1126/science.aea3381.

16. Fuzik, J., Zeisel, A., Máté, Z., Calvigioni, D., Yanagawa, Y., Szabó, G., Linnarsson, S., and Harkany, T. (2016). Integration of electrophysiological recordings with single-cell RNA-seq data identifies neuronal subtypes. Nat. Biotechnol. *34*, 175–183. https://doi.org/10.1038/nbt.3443.

17. Gao, Y., Dong, Q., Arachchilage, K.H., Risgaard, R.D., Syed, M., Sheng, J., Schmidt, D.K., Jin, T., Liu, S., Sandoval, S.O., et al. (2025). Multimodal analyses reveal genes driving electrophysiological maturation of neurons in the primate prefrontal cortex. Neuron. https://doi.org/10.1016/j.neuron.2025.04.025.

18. Sterin, I., Santos, A.C., and Park, S. (2022). Neuronal Activity Reporters as Drug Screening Platforms. Micromachines-basel *13*, 1500. https://doi.org/10.3390/mi13091500.

19. Lee, D., Hyun, J.H., Jung, K., Hannan, P., and Kwon, H.-B. (2017). A calcium- and light-gated switch to induce gene expression in activated neurons. Nat. Biotechnol. *35*, 858–863. https://doi.org/10.1038/nbt.3902.

20. Grienberger, C., and Konnerth, A. (2012). Imaging Calcium in Neurons. Neuron *73*, 862–885. https://doi.org/10.1016/j.neuron.2012.02.011.

21. Fosque, B.F., Sun, Y., Dana, H., Yang, C.-T., Ohyama, T., Tadross, M.R., Patel, R., Zlatic, M., Kim, D.S., Ahrens, M.B., et al. (2015). Neural circuits. Labeling of active neural circuits in vivo with designed calcium integrators. Sci. (N. York, NY) *347*, 755–760. https://doi.org/10.1126/science.1260922.

22. Edwards, K.A., Hoppa, M.B., and Bosco, G. (2020). The Photoconvertible Fluorescent Probe, CaMPARI, Labels Active Neurons in Freely-Moving Intact Adult Fruit Flies. Front. Neural Circuits *14*, 22. https://doi.org/10.3389/fncir.2020.00022.

23. Moeyaert, B., Holt, G., Madangopal, R., Perez-Alvarez, A., Fearey, B.C., Trojanowski, N.F., Ledderose, J., Zolnik, T.A., Das, A., Patel, D., et al. (2018). Improved methods for marking active neuron populations. Nat. Commun. *9*, 4440. https://doi.org/10.1038/s41467-018-06935-2.

24. Zolnik, T.A., Sha, F., Johenning, F.W., Schreiter, E.R., Looger, L.L., Larkum, M.E., and Sachdev, R.N.S. (2016). All-optical functional synaptic connectivity mapping in acute brain slices using the calcium integrator CaMPARI. J. Physiol. *595*, 1465–1477. https://doi.org/10.1113/jp273116.

25. Trojanowski, N.F., Bottorff, J., and Turrigiano, G.G. (2021). Activity labeling in vivo using CaMPARI2 reveals intrinsic and

synaptic differences between neurons with high and low firing rate set points. Neuron *109*, 663-676.e5. https://doi.org/10.1016/j.neuron.2020.11.027.

26. Das, A., Holden, S., Borovicka, J., Icardi, J., O'Niel, A., Chaklai, A., Patel, D., Patel, R., Petrie, S.K., Raber, J., et al. (2023). Large-scale recording of neuronal activity in freely-moving mice at cellular resolution. Nat. Commun. *14*, 6399. https://doi.org/10.1038/s41467-023-42083-y.

27. Tian, R., Gachechiladze, M.A., Ludwig, C.H., Laurie, M.T., Hong, J.Y., Nathaniel, D., Prabhu, A.V., Fernandopulle, M.S., Patel, R., Abshari, M., et al. (2019). CRISPR Interference-Based Platform for Multimodal Genetic Screens in Human iPSC-Derived Neurons. Neuron *104*, 239-255.e12. https://doi.org/10.1016/j.neuron.2019.07.014.

28. Wang, C., Ward, M.E., Chen, R., Liu, K., Tracy, T.E., Chen, X., Xie, M., Sohn, P.D., Ludwig, C., Meyer-Franke, A., et al. (2017). Scalable Production of iPSC-Derived Human Neurons to Identify Tau-Lowering Compounds by High-Content Screening. Stem Cell Rep. *9*, 1221–1233. https://doi.org/10.1016/j.stemcr.2017.08.019.

29. Zhang, Y., Pak, C., Han, Y., Ahlenius, H., Zhang, Z., Chanda, S., Marro, S., Patzke, C., Acuna, C., Covy, J., et al. (2013). Rapid Single-Step Induction of Functional Neurons from Human Pluripotent Stem Cells. Neuron *78*, 785–798. https://doi.org/10.1016/j.neuron.2013.05.029.

30. Shan, X., Zhang, A., Rezzonico, M.G., Tsai, M.-C., Sanchez-Priego, C., Zhang, Y., Chen, M.B., Choi, M., López, J.M.A., Phu, L., et al. (2024). Fully defined NGN2 neuron protocol reveals diverse signatures of neuronal maturation. Cell Rep. Methods *4*, 100858. https://doi.org/10.1016/j.crmeth.2024.100858.

31. Kosillo, P., Doig, N.M., Ahmed, K.M., Agopyan-Miu, A.H.C.W., Wong, C.D., Conyers, L., Threlfell, S., Magill, P.J., and Bateup, H.S. (2019). Tsc1-mTORC1 signaling controls striatal dopamine release and cognitive flexibility. Nat. Commun. *10*, 5426. https://doi.org/10.1038/s41467-019-13396-8.

32. Meijer, M., Dörr, B., Lammertse, H.C., Blithikioti, C., Weering, J.R. van, Toonen, R.F., Söllner, T.H., and Verhage, M. (2018). Tyrosine phosphorylation of Munc18-1 inhibits synaptic

transmission by preventing SNARE assembly. EMBO J. *37*, 300–320. https://doi.org/10.15252/embj.201796484.

33. Rao, V.R., and Lowenstein, D.H. (2015). Epilepsy. Curr. Biol. *25*, R742–R746. https://doi.org/10.1016/j.cub.2015.07.072.

34. Li, W., Xu, H., Xiao, T., Cong, L., Love, M.I., Zhang, F., Irizarry, R.A., Liu, J.S., Brown, M., and Liu, X.S. (2014). MAGeCK enables robust identification of essential genes from genome-scale CRISPR/Cas9 knockout screens. Genome Biol. *15*, 554. https://doi.org/10.1186/s13059-014-0554-4.

35. Oliver, K.L., Scheffer, I.E., Bennett, M.F., Grinton, B.E., Bahlo, M., and Berkovic, S.F. (2023). Genes4Epilepsy: An epilepsy gene resource. Epilepsia *64*, 1368–1375. https://doi.org/10.1111/epi.17547.

36. Mattison, K.A., Tossing, G., Mulroe, F., Simmons, C., Butler, K.M., Schreiber, A., Alsadah, A., Neilson, D.E., Naess, K., Wedell, A., et al. (2022). ATP6V0C variants impair V-ATPase function causing a neurodevelopmental disorder often associated with epilepsy. Brain *146*, 1357–1372. https://doi.org/10.1093/brain/awac330.

37. Bain, J.M., Cho, M.T., Telegrafi, A., Wilson, A., Brooks, S., Botti, C., Gowans, G., Autullo, L.A., Krishnamurthy, V., Willing, M.C., et al. (2016). Variants in HNRNPH2 on the X Chromosome Are Associated with a Neurodevelopmental Disorder in Females. Am. J. Hum. Genet. *99*, 728–734. https://doi.org/10.1016/j.ajhg.2016.06.028.

38. Suzuki, H., Yoshida, T., Morisada, N., Uehara, T., Kosaki, K., Sato, K., Matsubara, K., Takano-Shimizu, T., and Takenouchi, T. (2019). De novo NSF mutations cause early infantile epileptic encephalopathy. Ann. Clin. Transl. Neurol. *6*, 2334–2339. https://doi.org/10.1002/acn3.50917.

39. Schubert, J., Siekierska, A., Langlois, M., May, P., Huneau, C., Becker, F., Muhle, H., Suls, A., Lemke, J.R., Kovel, C.G.F. de, et al. (2014). Mutations in STX1B, encoding a presynaptic protein, cause fever-associated epilepsy syndromes. Nat. Genet. *46*, 1327–1332. https://doi.org/10.1038/ng.3130.

40. Fatima, A., Hoeber, J., Schuster, J., Koshimizu, E., Maya-Gonzalez, C., Keren, B., Mignot, C., Akram, T., Ali, Z., Miyatake, S., et al. (2021). Monoallelic and bi-allelic variants in NCDN cause

neurodevelopmental delay, intellectual disability, and epilepsy. Am. J. Hum. Genet. *108*, 739–748. https://doi.org/10.1016/j.ajhg.2021.02.015.

41. Jaworski, T., Banach-Kasper, E., and Gralec, K. (2019). GSK-3β at the Intersection of Neuronal Plasticity and Neurodegeneration. Neural Plast. *2019*, 4209475. https://doi.org/10.1155/2019/4209475.

42. Horn, S., Au, M., Basel-Salmon, L., Bayrak-Toydemir, P., Chapin, A., Cohen, L., Elting, M.W., Graham, J.M., Gonzaga-Jauregui, C., Konen, O., et al. (2019). De novo variants in PAK1 lead to intellectual disability with macrocephaly and seizures. Brain *142*, 3351–3359. https://doi.org/10.1093/brain/awz264.

43. Horváth, R., Abicht, A., Holinski-Feder, E., Laner, A., Gempel, K., Prokisch, H., Lochmüller, H., Klopstock, T., and Jaksch, M. (2006). Leigh syndrome caused by mutations in the flavoprotein (Fp) subunit of succinate dehydrogenase (SDHA). J. Neurol., Neurosurg. Psychiatry *77*, 74. https://doi.org/10.1136/jnnp.2005.067041.

44. Schoch, S., Deák, F., Königstorfer, A., Mozhayeva, M., Sara, Y., Südhof, T.C., and Kavalali, E.T. (2001). SNARE Function Analyzed in Synaptobrevin/VAMP Knockout Mice. Science *294*, 1117–1122. https://doi.org/10.1126/science.1064335.

45. Johnstone, D.L., Nguyen, T.T.M., Zambonin, J., Kernohan, K.D., St-Denis, A., Baratang, N.V., Hartley, T., Geraghty, M.T., Richer, J., Majewski, J., et al. (2020). Early infantile epileptic encephalopathy due to biallelic pathogenic variants in PIGQ: Report of seven new subjects and review of the literature. J. Inherit. Metab. Dis. *43*, 1321–1332. https://doi.org/10.1002/jimd.12278.

46. Kim, K., Park, I., Kim, J., Kang, M.-G., Choi, W.G., Shin, H., Kim, J.-S., Rhee, H.-W., and Suh, J.M. (2021). Dynamic tracking and identification of tissue-specific secretory proteins in the circulation of live mice. Nat. Commun. *12*, 5204. https://doi.org/10.1038/s41467-021-25546-y.

47. Stenmark, H. (2009). Rab GTPases as coordinators of vesicle traffic. Nat. Rev. Mol. Cell Biol. *10*, 513–525. https://doi.org/10.1038/nrm2728.

48. Shin, J., Nile, A., and Oh, J.-W. (2021). Role of adaptin protein complexes in intracellular trafficking and their impact on diseases.

Bioengineered *12*, 8259–8278. https://doi.org/10.1080/21655979.2021.1982846.

49. Liu, Q., Bautista-Gomez, J., Higgins, D.A., Yu, J., and Xiong, Y. (2021). Dysregulation of the AP2M1 phosphorylation cycle by LRRK2 impairs endocytosis and leads to dopaminergic neurodegeneration. Sci. Signal. *14*. https://doi.org/10.1126/scisignal.abg3555.

50. Mouret, R.Z., Greenbaum, J.P., Doll, H.M., Brody, E.M., Iacobucci, E.L., Roland, N.C., Simamora, R.C., Ruiz, I., Seymour, R., Ludwick, L., et al. (2024). The adaptor protein 2 (AP2) complex modulates habituation and behavioral selection across multiple pathways and time windows. iScience *27*, 109455. https://doi.org/10.1016/j.isci.2024.109455.

51. Howe, E.N., Burnette, M.D., Justice, M.E., Schnepp, P.M., Hedrick, V., Clancy, J.W., Guldner, I.H., Lamere, A.T., Li, J., Aryal, U.K., et al. (2020). Rab11b-mediated integrin recycling promotes brain metastatic adaptation and outgrowth. Nat. Commun. *11*, 3017. https://doi.org/10.1038/s41467-020-16832-2.

52. Kang, H., Han, A., Zhang, A., Jeong, H., Koh, W., Lee, J.M., Lee, H., Jo, H.Y., Maria-Solano, M.A., Bhalla, M., et al. (2024). GolpHCat (TMEM87A), a unique voltage-dependent cation channel in Golgi apparatus, contributes to Golgi-pH maintenance and hippocampus-dependent memory. Nat. Commun. *15*, 5830. https://doi.org/10.1038/s41467-024-49297-8.

53. Stoetzel, C., Bär, S., Craene, J.-O.D., Scheidecker, S., Etard, C., Chicher, J., Reck, J.R., Perrault, I., Geoffroy, V., Chennen, K., et al. (2016). A mutation in VPS15 (PIK3R4) causes a ciliopathy and affects IFT20 release from the cis-Golgi. Nat. Commun. *7*, 13586. https://doi.org/10.1038/ncomms13586.

54. Koike, S., and Jahn, R. (2019). SNAREs define targeting specificity of trafficking vesicles by combinatorial interaction with tethering factors. Nat. Commun. *10*, 1608. https://doi.org/10.1038/s41467-019-09617-9.

55. Babst, M., Katzmann, D.J., Estepa-Sabal, E.J., Meerloo, T., and Emr, S.D. (2002). Escrt-III An endosome-associated heterooligomeric protein complex required for mvb sorting. Dev. Cell *3*, 271–282. https://doi.org/10.1016/s1534-5807(02)00220-4.

56. Azmi, I.F., Davies, B.A., Xiao, J., Babst, M., Xu, Z., and Katzmann, D.J. (2008). ESCRT-III Family Members Stimulate Vps4 ATPase Activity Directly or via Vta1. Dev. Cell *14*, 50–61. https://doi.org/10.1016/j.devcel.2007.10.021.

57. Migliano, S.M., Schultz, S.W., Wenzel, E.M., Takáts, S., Liu, D., Mørk, S., Tan, K.W., Rusten, T.E., Raiborg, C., and Stenmark, H. (2023). Removal of hypersignaling endosomes by simaphagy. Autophagy *20*, 769–791. https://doi.org/10.1080/15548627.2023.2267958.

58. Schluter, C., Lam, K.K.Y., Brumm, J., Wu, B.W., Saunders, M., Stevens, T.H., Bryan, J., and Conibear, E. (2008). Global Analysis of Yeast Endosomal Transport Identifies the Vps55/68 Sorting Complex. Mol. Biol. Cell *19*, 1282–1294. https://doi.org/10.1091/mbc.e07-07-0659.

59. Alsleben, S., and Kölling, R. (2022). Vps68 cooperates with ESCRT-III in intraluminal vesicle formation. J. Cell Sci. *135*. https://doi.org/10.1242/jcs.259743.

60. Longva, K.E., Blystad, F.D., Stang, E., Larsen, A.M., Johannessen, L.E., and Madshus, I.H. (2002). Ubiquitination and proteasomal activity is required for transport of the EGF receptor to inner membranes of multivesicular bodies. J. Cell Biol. *156*, 843–854. https://doi.org/10.1083/jcb.200106056.

61. Hurley, J.H., Coyne, A.N., Miączyńska, M., and Stenmark, H. (2025). The expanding repertoire of ESCRT functions in cell biology and disease. Nature *642*, 877–888. https://doi.org/10.1038/s41586-025-08950-y.

62. Neefjes, J., Jongsma, M.M.L., and Berlin, I. (2017). Stop or Go? Endosome Positioning in the Establishment of Compartment Architecture, Dynamics, and Function. Trends Cell Biol. *27*, 580–594. https://doi.org/10.1016/j.tcb.2017.03.002.

63. Im, Y.J., Wollert, T., Boura, E., and Hurley, J.H. (2009). Structure and Function of the ESCRT-II-III Interface in Multivesicular Body Biogenesis. Dev. Cell *17*, 234–243. https://doi.org/10.1016/j.devcel.2009.07.008.

64. Stuffers, S., Wegner, C.S., Stenmark, H., and Brech, A. (2009). Multivesicular Endosome Biogenesis in the Absence of ESCRTs.

Traffic *10*, 925–937. https://doi.org/10.1111/j.1600-0854.2009.00920.x.

65. Piper, R.C., and Katzmann, D.J. (2007). Biogenesis and Function of Multivesicular Bodies. Cell Dev. Biol. *23*, 519–547. https://doi.org/10.1146/annurev.cellbio.23.090506.123319.

66. Bartheld, C.S.V., and Altick, A.L. (2011). Multivesicular bodies in neurons: Distribution, protein content, and trafficking functions. Prog. Neurobiol. *93*, 313–340. https://doi.org/10.1016/j.pneurobio.2011.01.003.

67. Cadwell, C.R., Palasantza, A., Jiang, X., Berens, P., Deng, Q., Yilmaz, M., Reimer, J., Shen, S., Bethge, M., Tolias, K.F., et al. (2016). Electrophysiological, transcriptomic and morphologic profiling of single neurons using Patch-seq. Nat. Biotechnol. *34*, 199–203. https://doi.org/10.1038/nbt.3445.

68. Vardar, G., Chang, S., Arancillo, M., Wu, Y.-J., Trimbuch, T., and Rosenmund, C. (2016). Distinct Functions of Syntaxin-1 in Neuronal Maintenance, Synaptic Vesicle Docking, and Fusion in Mouse Neurons. J. Neurosci. *36*, 7911–7924. https://doi.org/10.1523/jneurosci.1314-16.2016.

69. Kölling, R. (2024). Interaction between ESCRT-III proteins and the yeast SERINC homolog Tms1. GENETICS *228*, iyae132. https://doi.org/10.1093/genetics/iyae132.

70. Picon, C., Aleksynas, R., Wojewska, M., Virgiliis, F. de, Merkler, D., and Reynolds, R. (2025). Dysregulation of the endosomal sorting complex III is linked to neurodegeneration in progressive multiple sclerosis. Brain Pathol. *36*, e70034. https://doi.org/10.1111/bpa.70034.

71. Coulter, M.E., Dorobantu, C.M., Lodewijk, G.A., Delalande, F., Cianferani, S., Ganesh, V.S., Smith, R.S., Lim, E.T., Xu, C.S., Pang, S., et al. (2018). The ESCRT-III Protein CHMP1A Mediates Secretion of Sonic Hedgehog on a Distinctive Subtype of Extracellular Vesicles. Cell Rep. *24*, 973-986.e8. https://doi.org/10.1016/j.celrep.2018.06.100.

72. Lee, J.-A., Beigneux, A., Ahmad, S.T., Young, S.G., and Gao, F.-B. (2007). ESCRT-III Dysfunction Causes Autophagosome

Accumulation and Neurodegeneration. Curr. Biol. *17*, 1561–1567. https://doi.org/10.1016/j.cub.2007.07.029.

73. Boggess, S.C., Gandhi, V., Tsai, M.-C., Marzette, E., Teyssier, N., Chou, J.Y.-Y., Hu, X., Cramer, A., Yadanar, L., Shroff, K., et al. (2025). A Massively Parallel CRISPR-Based Screening Platform for Modifiers of Neuronal Activity. bioRxiv, 2024.02.28.582546. https://doi.org/10.1101/2024.02.28.582546.

74. Beaudoin, G.M.J., Lee, S.-H., Singh, D., Yuan, Y., Ng, Y.-G., Reichardt, L.F., and Arikkath, J. (2012). Culturing pyramidal neurons from the early postnatal mouse hippocampus and cortex. Nat. Protoc. *7*, 1741–1754. https://doi.org/10.1038/nprot.2012.099.

75. Labun, K., Montague, T.G., Krause, M., Cleuren, Y.N.T., Tjeldnes, H., and Valen, E. (2019). CHOPCHOP v3: expanding the CRISPR web toolbox beyond genome editing. Nucleic Acids Res. *47*, W171–W174. https://doi.org/10.1093/nar/gkz365.

76. Zeng, Q., Li, Y., Wu, Y., Wu, J., Xu, K., Chen, Y., Rao, Y., Li, N., Luo, Y., Jiang, C., et al. (2025). Neuropeptide Y neurons mediate opioid-induced itch by disinhibiting GRP-GRPR microcircuits in the spinal cord. Nat. Commun. *16*, 7074. https://doi.org/10.1038/s41467-025-62382-w.

77. Shan, L., Xu, K., Ji, L., Zeng, Q., Liu, Y., Wu, Y., Chen, Y., Li, Y., Hu, Q., Wu, J., et al. (2024). Injured sensory neurons-derived galectin-3 contributes to neuropathic pain via programming microglia in the spinal dorsal horn. Brain, Behav., Immun. *117*, 80–99. https://doi.org/10.1016/j.bbi.2024.01.002.

78. Petkovic, M., Oses-Prieto, J., Burlingame, A., Jan, L.Y., and Jan, Y.N. (2020). TMEM16K is an interorganelle regulator of endosomal sorting. Nat. Commun. *11*, 3298. https://doi.org/10.1038/s41467-020-17016-8.

79. Hale, W.D., Südhof, T.C., and Huganir, R.L. (2023). Engineered adhesion molecules drive synapse organization. Proc. Natl. Acad. Sci. *120*, e2215905120. https://doi.org/10.1073/pnas.2215905120.

80. Kraeuter, A.-K., Guest, P.C., and Sarnyai, Z. (2018). The Open Field Test for Measuring Locomotor Activity and Anxiety-Like Behavior. Methods Mol. Biol. (Clifton, NJ) *1916*, 99–103. https://doi.org/10.1007/978-1-4939-8994-2_9.

81. Wang, G., Peng, S., Mendez, M.R., Keramidas, A., Castellano, D., Wu, K., Han, W., Tian, Q., Dong, L., Li, Y., et al. (2024). The TMEM132B-GABAA receptor complex controls alcohol actions in the brain. Cell *187*, 6649-6668.e35. https://doi.org/10.1016/j.cell.2024.09.006.

82. Hallgren, J., Tsirigos, K.D., Pedersen, M.D., Armenteros, J.J.A., Marcatili, P., Nielsen, H., Krogh, A., and Winther, O. (2022). DeepTMHMM predicts alpha and beta transmembrane proteins using deep neural networks. https://doi.org/10.1101/2022.04.08.487609.

ACKNOWLEDGEMENTS

We thank the assistance of SUSTech Core Research Facilities on flow cytometry. We also would like to acknowledge the SZBL Bio-Imaging core for assistance with the SEM sample preparation and imaging. This work was supported by the National Key Research and Development Program of China (2024YFA0919800), Shenzhen Medical Research Fund (A2303039), Guangdong Basic and Applied Basic Research Foundation (2023B1515020075), the Key Area Research and Development Program of Guangdong Province (2023B0303010002), National Natural Science Foundation of China (82171416, 32300802), Shenzhen Fundamental Research Program (JCYJ20220530112602006 and RCYX20221008092845052) and Lingang Laboratory Grant (LGL-3142-ADB24020).

AUTHOR CONTRIBUTION

R.T. and X. J. conceived the project. J.W. established the CaMPARI2 system in iNeurons, performed the screen, and carried out validation and mechanistic studies with assistance from X.Z. and guidance from R.T. X. J. designed and guided the synapse phenotype experiments and behavioral tests. M.L. and J.C. characterized phenotypes associated with Tmem50a loss in primary mouse neurons. M.L. performed SEM experiments and mouse behavioral tests. Y.C. conducted electrophysiology experiments and related analyses under the guidance of Z.W. J.W., M.L., and R.T. wrote the manuscript with input from all authors.

COMPETING INTERESTS

The authors declare no competing interests.

SUPPLEMENTAL INFORMATION

Supplementary Data 1: sgRNA protospacer sequences for the memory-associated gene library

Supplementary Data 2: sgRNA counts and MAGeCK-iNC analysis results from the CaMPARI2-CRISPRi screen

Supplementary Data 3: sgRNA and primer sequences used in this study

Supplementary Data 4: TMEM50A interactome identified by IP-MS

Supplementary Data 5: Surface proteome comparing *TMEM50A* KO and WT iNeurons

FIGURES AND FIGURE LEGENDS

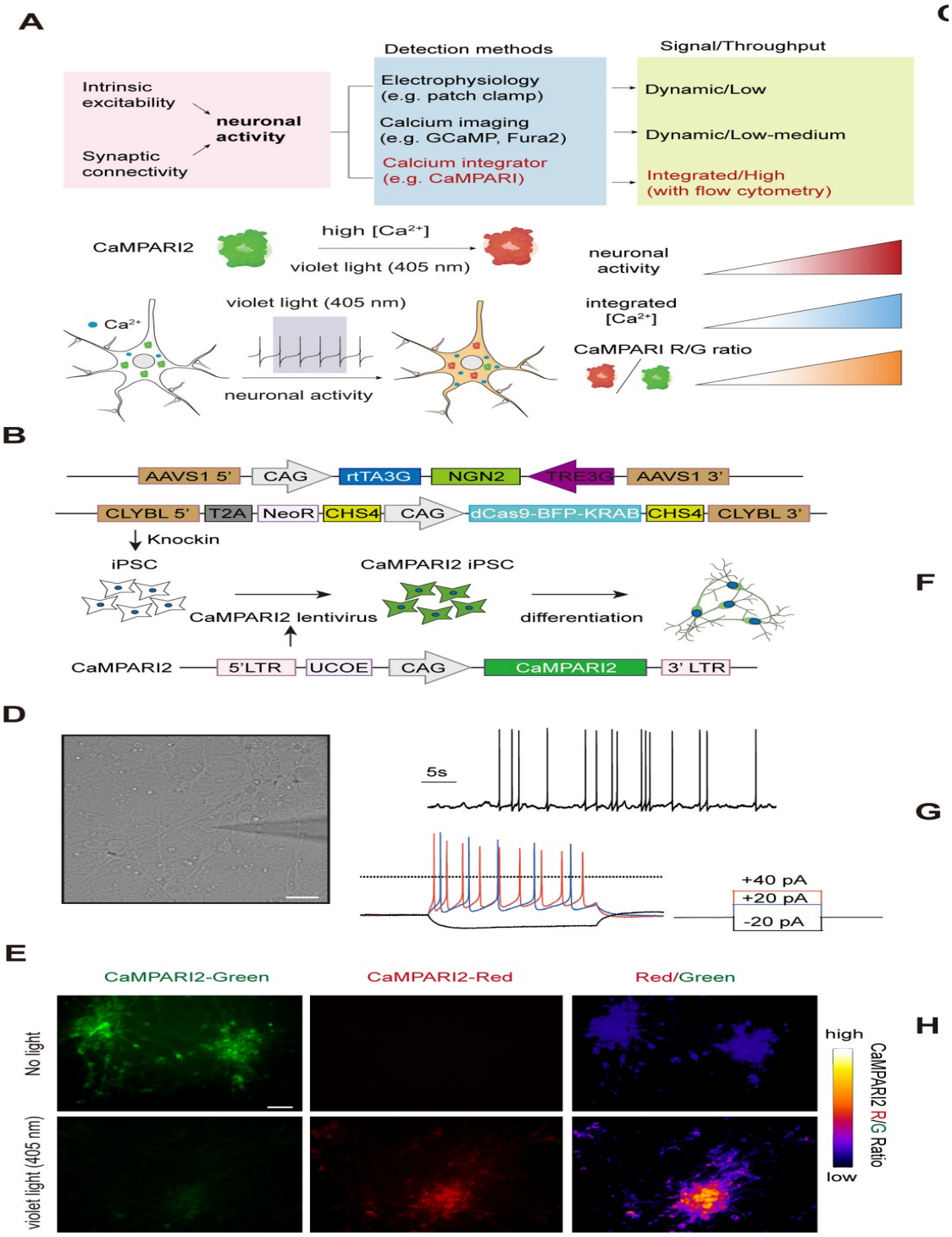

Figure 1. Establishment of a CaMPARI2-based high-throughput platform for quantifying neuronal activity in human iNeurons

(A) Schematic comparison of major approaches for measuring

neuronal activity. Electrophysiology provides gold-standard but low-throughput measurements; calcium and voltage imaging capture transient activity in low- to medium-throughput arrayed formats; CaMPARI2 converts cumulative Ca^{2+} activity during a defined illumination window into a stable red/green fluorescence ratio that can be quantified at single-cell resolution by flow cytometry, enabling pooled genetic screening.

(B) Strategy for integrating CaMPARI2 into the CRISPRi iNeuron platform. Human iPSCs carry a doxycycline-inducible NGN2 cassette at the AAVS1 locus and a dCas9-BFP-KRAB cassette at the CLYBL locus. CaMPARI2 is introduced by lentiviral transduction under a CAG promoter. Upon doxycycline induction, iPSCs rapidly differentiate into glutamatergic iNeurons expressing CaMPARI2 and CRISPRi machinery.

(C) Transcriptomic maturation of iNeurons. Heatmap showing expression dynamics of representative neuronal activity–related genes (including ion channels, glutamate receptors, vesicle release machinery, and synaptic components) across days 14, 21, 28, and 35 of differentiation. Expression of activity-associated genes increases after day 14 and plateaus around days 21–28.

(D) Functional maturation of iNeurons by electrophysiology. Left, DIC image of day 28 iNeurons (scale bar, 10 μm). Right, representative traces of spontaneous (top) and evoked (bottom) action potential in day 28 iNeurons.

(E) Representative confocal images of CaMPARI2-iNeurons before and after 5 min of 405 nm violet light illumination. Panels show green fluorescence, red fluorescence, and green-to-red ratio. Scale bar: 10 μm.

(F) Quantification of CaMPARI2 photoconversion by flow cytometry

as a function of illumination time. CaMPARI2 red-to-green (R/G) fluorescence ratio increases with longer illumination duration (0–10 min). Data are presented as mean ± SD. n = 3 biological replicates per condition.

(G) Dose-dependent increase in CaMPARI2 R/G ratio upon glutamate stimulation. iNeurons were treated with increasing concentrations of glutamate (0–100 µM) for 5 min during violet light illumination. Data are presented as mean ± SD. n = 3 biological replicates per condition.

(H) CaMPARI2 detects genetically driven changes in neuronal activity. Quantification of CaMPARI2 R/G ratio in control iNeurons (NTC) versus iNeurons with CRISPRi-mediated knockdown of *TSC1* or *STXBP1* under 1 min (left) or 5 min (right) illumination. Data are presented as mean ± SD. n = 3 biological replicates per condition.

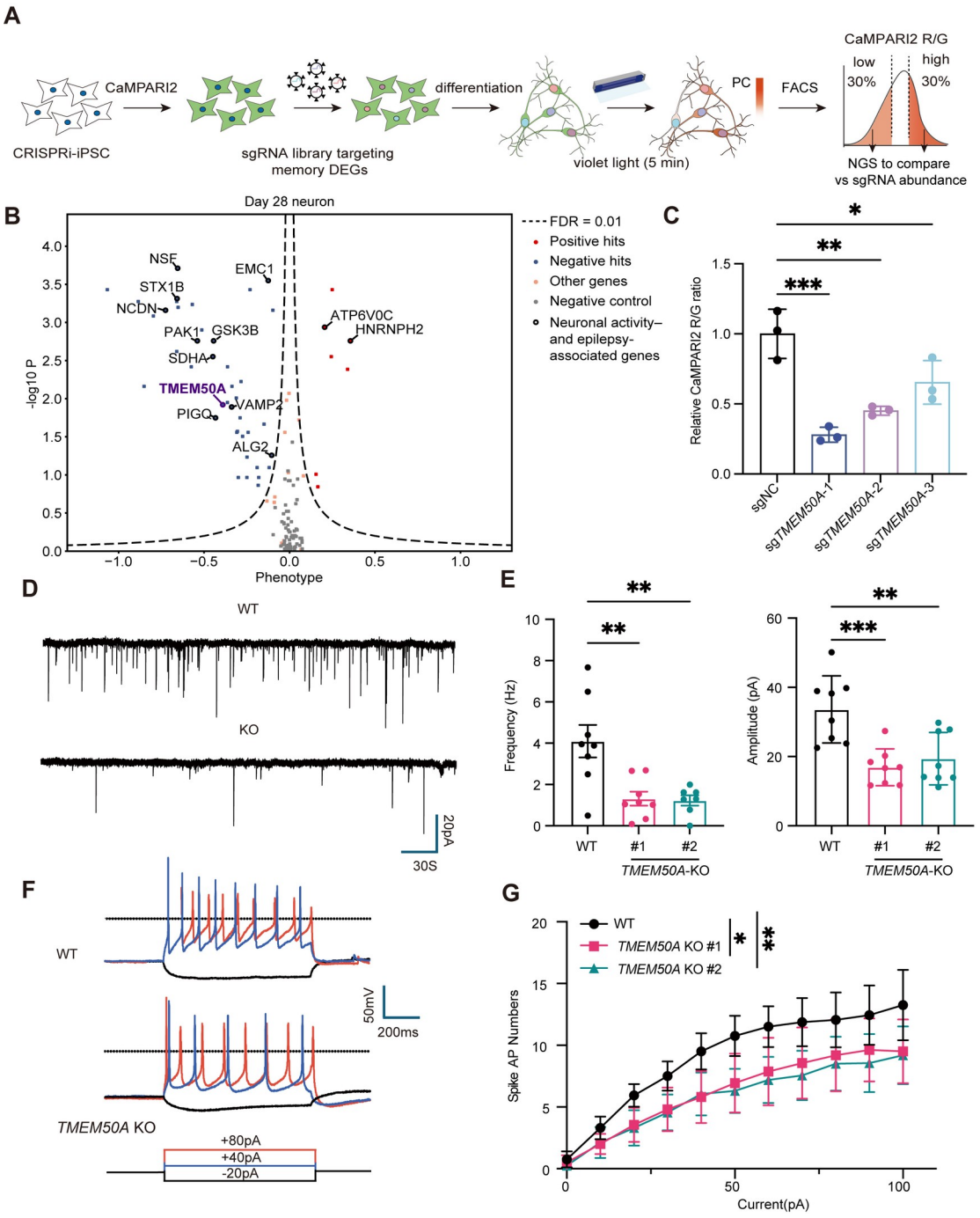

Figure 2. A CaMPARI2-based CRISPRi screen identifies TMEM50A as an essential regulator of neuronal activity

(A) Schematic of the CaMPARI2-CRISPRi screening workflow. CRISPRi-iPSCs expressing CaMPARI2 were transduced with an sgRNA library targeting memory-associated DEGs. Following differentiation into iNeurons, cells were subjected to 5 min of violet

light photoconversion (PC), dissociated, and sorted by FACS based on CaMPARI2 red-to-green (R/G) ratio. The top 30% (high activity) and bottom 30% (low activity) populations were collected, and sgRNA representation was quantified by next-generation sequencing (NGS) to identify hits.

(B) Volcano plot showing the CaMPARI2 screen results. The x axis indicates the activity phenotype score (negative values, decreased CaMPARI2 signal upon knockdown; positive values, increased signal), and the y axis indicates $-\log_{10}$ P from MAGeCK-iNC analysis. Dashed line marks FDR = 0.01. Selected known neuronal activity– and epilepsy-associated genes are labeled. *TMEM50A*, a gene of previously unknown function, is highlighted in purple.

(C) Validation of *TMEM50A* as a negative hit from the screen. Relative CaMPARI2 R/G ratio in iNeurons transduced with non-targeting control sgRNA (sgNTC) or three independent sgRNAs targeting *TMEM50A* (sgTMEM50A-1, -2, -3). Data are normalized to sgNTC and presented as mean ± SD (n = 3 biological replicates). *p < 0.05, **p < 0.01, ***p < 0.001, one-way ANOVA.

(D–E) *TMEM50A* loss impairs excitatory synaptic transmission. (D) Representative voltage-clamp traces of sEPSCs in WT and *TMEM50A* KO iNeurons. Scale bars: 20 pA, 30 s. (E) Quantification of sEPSC frequency (left) and amplitude (right) in WT and two independent *TMEM50A* KO lines (#1, #2). Each dot represents one cell. Data are presented as mean ± SEM (n = 8 neurons). *p < 0.05, **p < 0.01, ***p < 0.001, one-way ANOVA.

(F–G) *TMEM50A* loss reduces intrinsic excitability. (F) Representative current-clamp recordings showing action potential firing in response to current injections (−20, +40, +80 pA; 300 ms) in WT and *TMEM50A* KO iNeurons. Scale bars: 50 mV, 200 ms. (G)

Input–output curves showing the number of action potentials evoked as a function of injected current for WT and *TMEM50A* KO (#1, #2) iNeurons. Data are presented as mean ± SEM (n = 16 neurons). *p < 0.05, **p < 0.01, Two-way ANOVA Bonferroni's multiple comparisons.

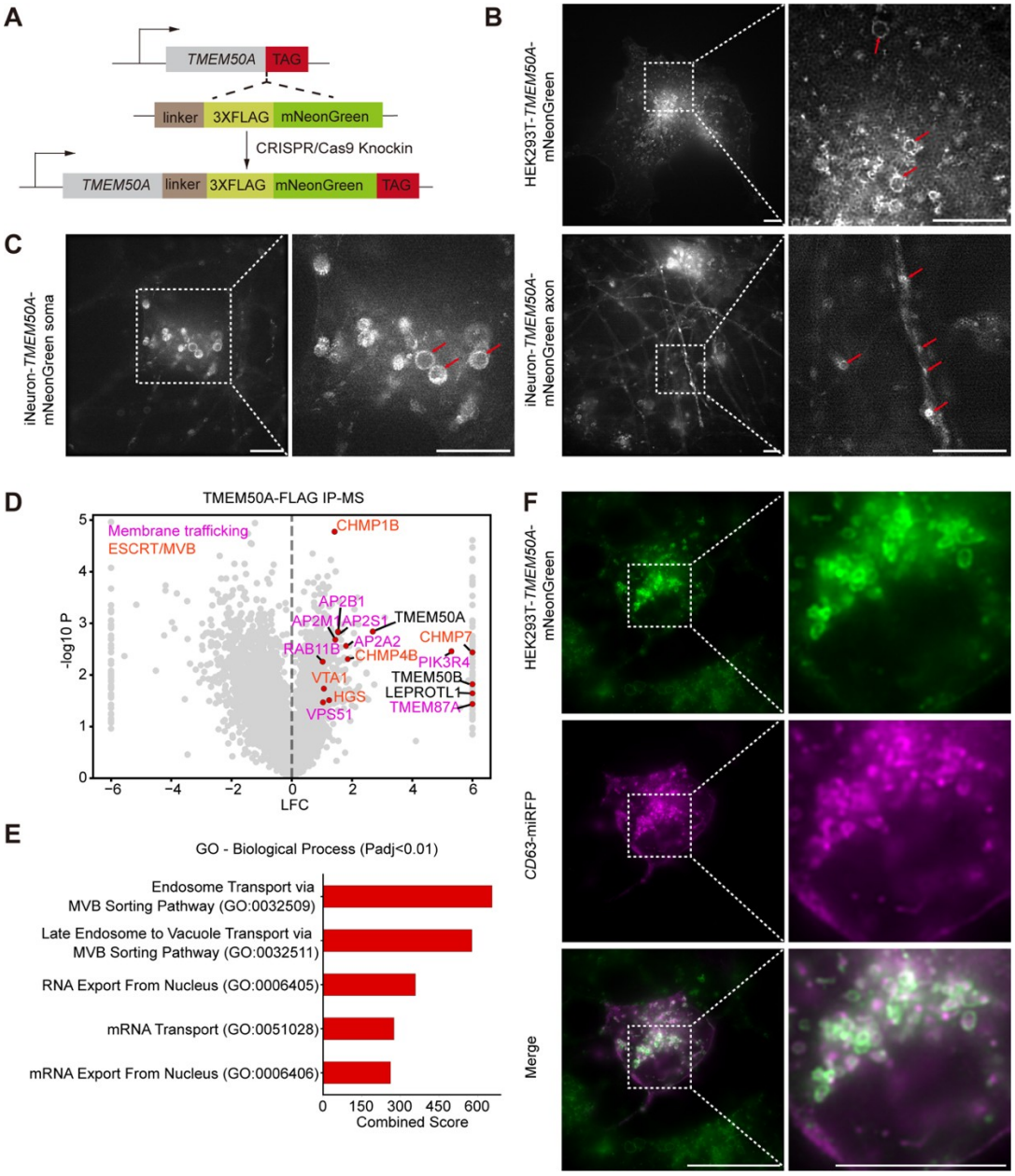

Figure 3. TMEM50A localizes to multivesicular bodies

(A) Schematic of CRISPR/Cas9-mediated endogenous tagging strategy. A C-terminal 3×FLAG–mNeonGreen cassette was inserted

in-frame at the TMEM50A locus to generate TMEM50A–3×FLAG–mNeonGreen knock-in (KI) cells.

(B–C) Super-resolution imaging of endogenously tagged TMEM50A–mNeonGreen. TMEM50A shows a punctate, vesicular distribution in HEK293T KI cells and in iNeurons, with TMEM50A-positive vesicles present in both soma and neurites. Magnified views highlight representative TMEM50A-positive vesicles (red arrows). Scale bars, 5 µm.

(D) Volcano plot of proteins identified by TMEM50A–FLAG immunoprecipitation–mass spectrometry (IP–MS) in iNeurons. The x axis shows $\log_2$ fold change (LFC) relative to IgG control and the y axis shows $-\log_{10}$ P. TMEM50A and selected enriched interactors involved in membrane trafficking (magenta) and ESCRT/MVB function (orange) are labeled.

(E) Gene Ontology (GO) enrichment analysis of TMEM50A interactors (Padj < 0.01).

(F) Co-localization of TMEM50A with the MVB marker CD63. Representative confocal images of HEK293T TMEM50A–mNeonGreen KI cells (green) co-expressing CD63–miRFP (magenta). Scale bars, 5 µm.

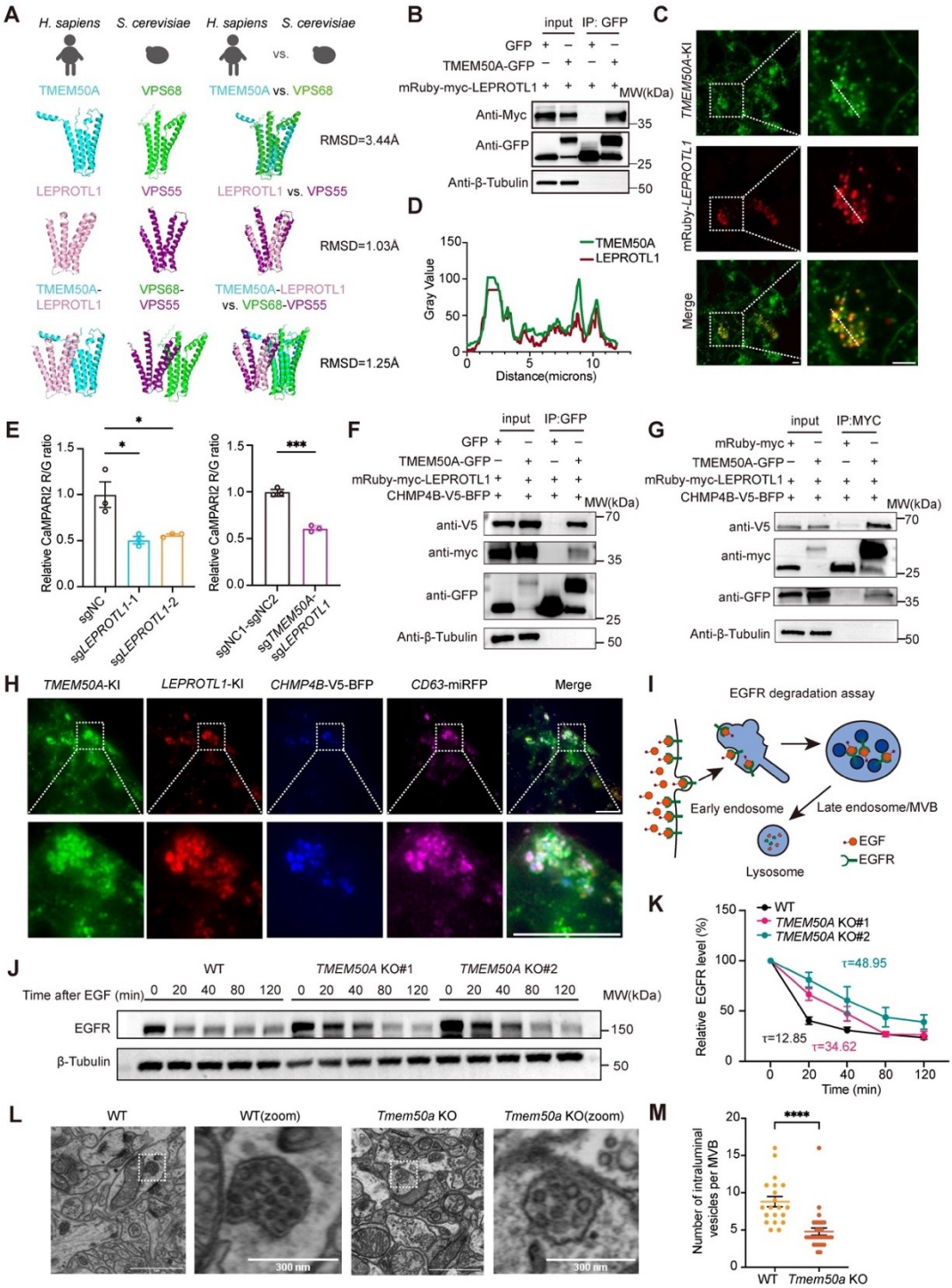

Figure 4. TMEM50A forms a complex with LEPROTL1 and ESCRT-III to support MVB function

(A) Structural conservation of the TMEM50A–LEPROTL1 complex. AlphaFold3-based models of human TMEM50A and LEPROTL1 and their yeast homologs Vps68 and Vps55, shown individually and as

complexes.

(B) Co-immunoprecipitation (co-IP) showing interaction between TMEM50A and LEPROTL1. HEK293T cells expressing TMEM50A-GFP and mRuby-myc–LEPROTL1 were subjected to GFP immunoprecipitation followed by immunoblotting with anti-Myc and anti-GFP; β-tubulin, loading control.

(C–D) Co-localization of TMEM50A and LEPROTL1 in cells. (C) Representative fluorescence images of TMEM50A knock-in (KI) cells expressing mRuby-myc–LEPROTL1; Scale bars, 5 μm. (D) Line-scan intensity profiles across the indicated region show correlated TMEM50A and LEPROTL1 signals.

(E) Functional epistasis analysis. CaMPARI2 R/G ratio in iNeurons with CRISPRi-mediated knockdown of *LEPROTL1* individually (left) or in combination with *TMEM50A* (right). Double knockdown does not enhance the phenotype relative to single knockdowns, indicating that TMEM50A and LEPROTL1 function in the same pathway. Relative R/G ratios normalized to control sgRNA are shown as mean ± SD (n = 3 biological replicates). *p < 0.05, **p < 0.01, ***p < 0.001, One-way ANOVA.

(F–G) Co-IP demonstrating interactions among TMEM50A, LEPROTL1, and the ESCRT-III component CHMP4B. (F) Anti-GFP IP from cells co-expressing mRuby–myc, TMEM50A–GFP, mRuby–myc–LEPROTL1, and CHMP4B–V5–BFP. (G) Anti-Myc IP from cells co-expressing the same constructs.

(H) Co-localization of TMEM50A, LEPROTL1, CHMP4B, and CD63 at MVBs. Representative confocal images of cells co-expressing TMEM50A–mNeonGreen (green), LEPROTL1–mRuby (red), CHMP4B–V5–BFP (blue), and CD63–mRFP (magenta). Scale bars, 5 μm.

(I) Schematic of the EGFR degradation assay.

(J–K) TMEM50A is required for efficient EGFR degradation. (J) Time-course Western blots of EGFR levels following EGF stimulation in WT and two independent *TMEM50A* knockout (KO#1, KO#2) HEK293T cell lines; β-Tubulin serves as a loading control. (K) Quantification of relative EGFR levels (normalized to time 0) plotted over time KO cells show a slower EGFR degradation rate compared to WT cells. The decay rates (τ) for each condition are indicated on the graph. Data are presented as mean ± SEM (n = 3 biological replicates).

(L–M) *Tmem50a* loss reduces intraluminal vesicle (ILV) formation in MVBs *in vivo*. (L) Representative scanning electron microscopy (SEM) images of MVBs from the anterior cingulate cortex (ACC) of WT and *Tmem50a*-KO mice. Scale bars, as indicated. (M) Quantification of ILV number per MVB. Each dot represents one MVB; Data are presented as mean ± SEM (WT: n = 20; *Tmem50a*-KO: n = 29). ****$p < 0.0001$, one-way ANOVA.

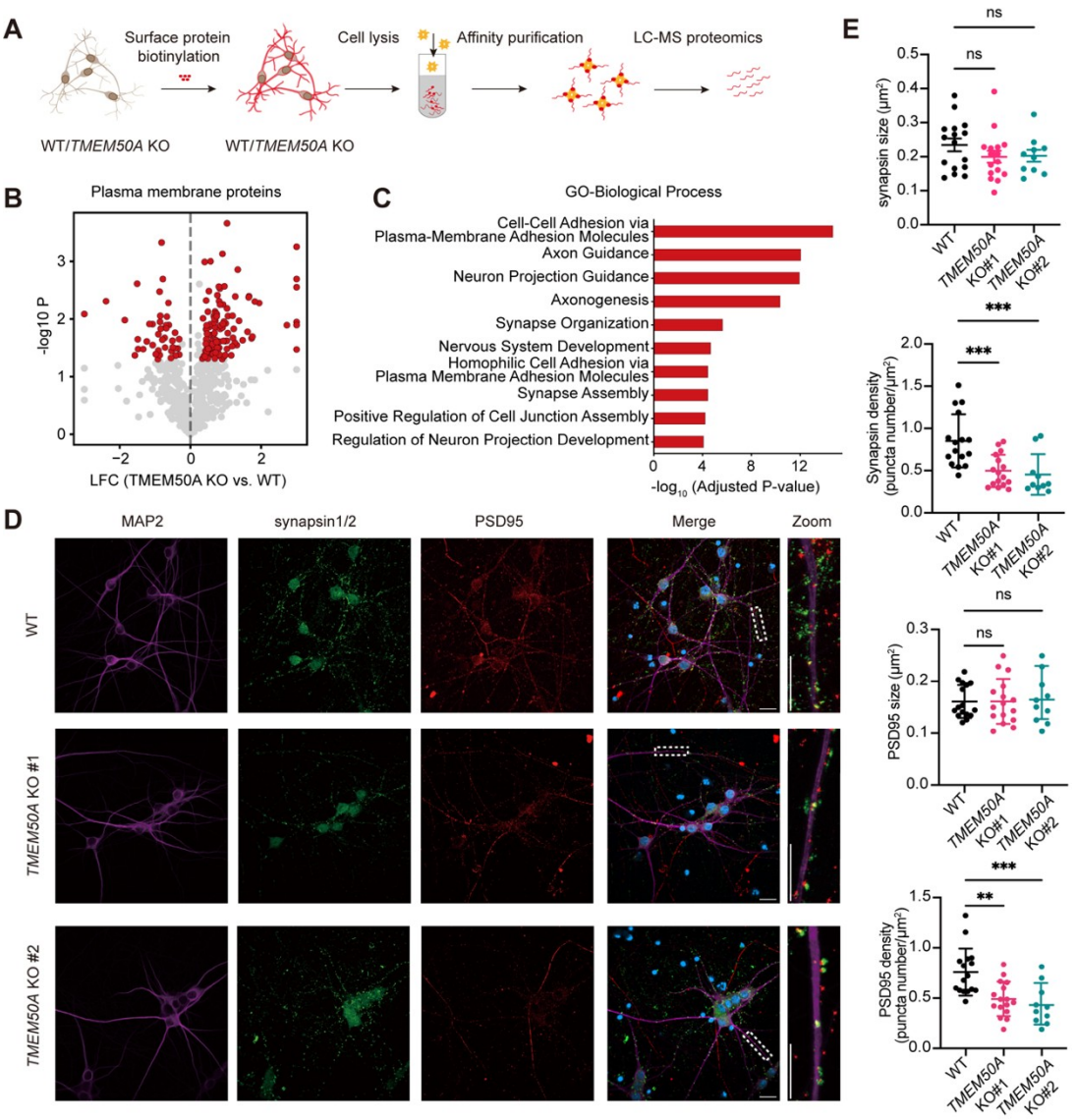

Figure 5. *TMEM50A* loss remodels the neuronal surface proteome and reduces synapse density in human iNeurons

(A) Schematic of the surface proteomics workflow. WT and *TMEM50A* KO iNeurons were subjected to cell-surface protein biotinylation, followed by cell lysis, affinity purification of biotinylated proteins, and LC–MS/MS analysis.

(B) Volcano plot of plasma membrane proteins comparing *TMEM50A* KO versus WT iNeurons. Significantly altered surface proteins are highlighted in red.

(C) Gene Ontology (GO) enrichment analysis (Biological Process) of

significantly changed surface proteins in *TMEM50A* KO neurons. Top 10 significantly enriched terms are shown.

(D) Representative confocal images of WT and *TMEM50A* KO iNeuron lines stained for MAP2 (dendrites, purple), synapsin1/2 (presynaptic marker, green), and PSD95 (postsynaptic marker, red). Merged and zoomed views (right) show synaptic puncta along MAP2 dendrites. Scale bars, 10 μm.

(E) Quantification of synaptic puncta. Top: synapsin1/2 puncta size per neuron; second: synapsin1/2 puncta density per μm dendrite length; third: PSD95 puncta size; bottom: PSD95 puncta density. Data are presented as mean ± SEM (WT: $n = 16$; *TMEM50A* KO #1: n= 16; *TMEM50A* KO #2: n=10). ns, not significant, $^{**}p < 0.01$, $^{***}p < 0.001$, one-way ANOVA.

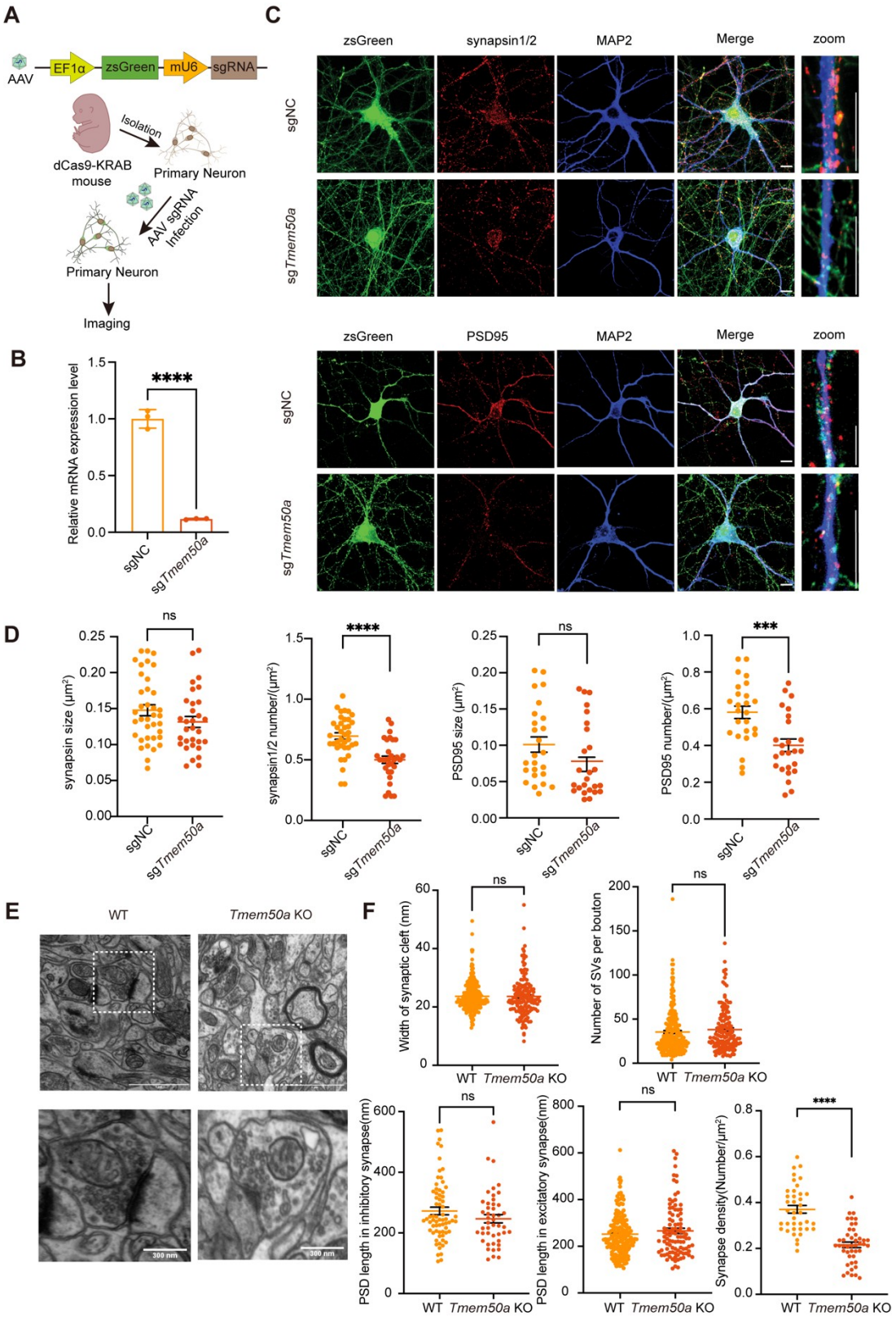

Figure 6. *Tmem50a* loss decreases synapse density in primary neurons and *in vivo*

(A) Schematic of CRISPRi-mediated knockdown of *Tmem50a* in primary cortical neurons. Primary neurons from dCas9-KRAB mice were infected with AAV expressing either a non-targeting control sgRNA (sgNC) or a *Tmem50a*-targeting sgRNA together with zsGreen for labeling.

(B) qRT-PCR validation of *Tmem50a* knockdown efficiency in primary neurons transduced with sg*Tmem50a* compared with sgNC. Data are presented as mean ± SD (n = 3 biological replicates). **** P < 0.0001, unpaired t test.

(C) Representative immunofluorescence images of sgNC and sg*Tmem50a* primary neurons stained for synapsin1/2 (up, red) or PSD95 (bottom, red) together with MAP2 (blue), with zoomed-in views showing synaptic puncta. zsGreen, infection marker. Scale bars: 10 μm.

(D) Quantification of Synapsin1/2 and PSD95 puncta density and size in sgNC and sg*Tmem50a* neurons. Data are presented as mean ± SEM (synapsin1/2 sgNC: n = 37, sg*Tmem50a*: n = 31; PSD95 sgNC: n = 25, sg*Tmem50a*: n = 25). ns, not significant, ***p < 0.001, ****p < 0.0001, unpaired t test.

(E) Representative electron microscopy images of the ultrastructural of synapse in the ACC region of WT and *Tmem50a*-KO mouse brain tissue. Scale bars, as indicated.

(F) Quantification of synaptic cleft width (WT n = 237, KO n =146), synaptic vesicle (SV) number per bouton (WT n = 233, KO n =151), PSD length at inhibitory (WT n = 64, KO n =48) and excitatory synapses (WT n = 175, KO n = 100), and synapse density (WT n = 38, KO n = 45) in the ACC region of WT and *Tmem50a*-KO mouse brain tissue. Data are presented as mean ± SEM. ns, not significant, ****p <0.0001, unpaired t-test.

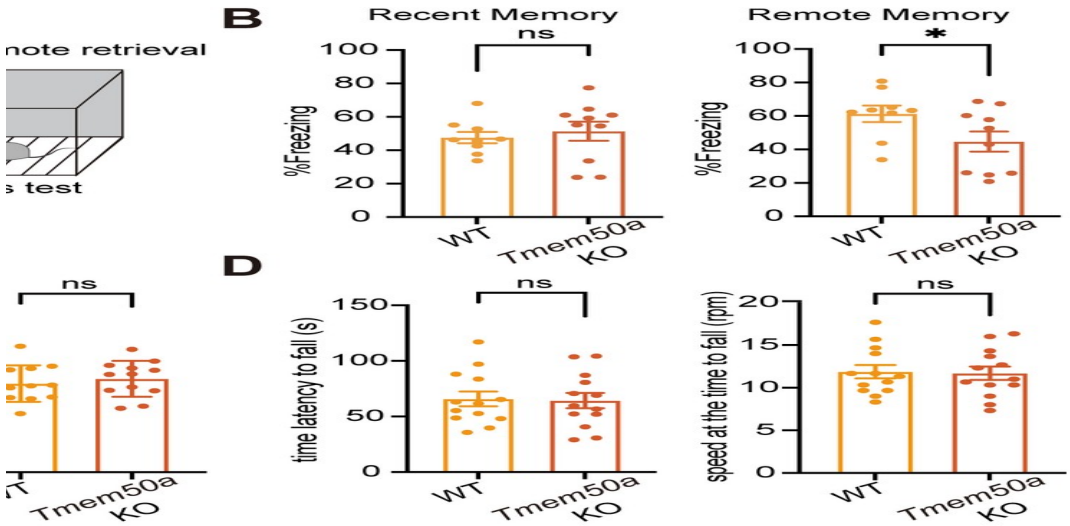

Figure 7. *Tmem50a* loss impairs remote memory and alters anxiety-like behavior without affecting motor coordination

(A) Schematic of the contextual fear conditioning paradigm.

(B) Freezing behavior during recent (Day 5) and remote (Day 21) memory retrieval. *Tmem50a*-KO mice show normal recent memory but significantly reduced freezing during remote memory retrieval compared with WT controls. Data are presented as mean ± SEM (WT mice: n = 9, KO mice: n = 10). ns, not significant, *p <0.05, unpaired t test.

(C) Open field test. Left: representative locomotor traces of WT and *Tmem50a*-KO mice (central zone outlined in green). Right: quantification of time spent in the central zone and total distance traveled. *Tmem50a*-KO mice spend more time in the center (reduced anxiety-like behavior) with no change in total distance. Data are presented as mean ± SEM (n =12). ns, not significant, *p <0.05, unpaired t test.

(D) Rotarod test. Latency to fall and speed at the time of fall are shown for WT and *Tmem50a*-KO mice. No significant differences were observed, indicating normal motor coordination and balance.

Data are presented as mean ± SEM (n=13). ns, not significant, unpaired t test.

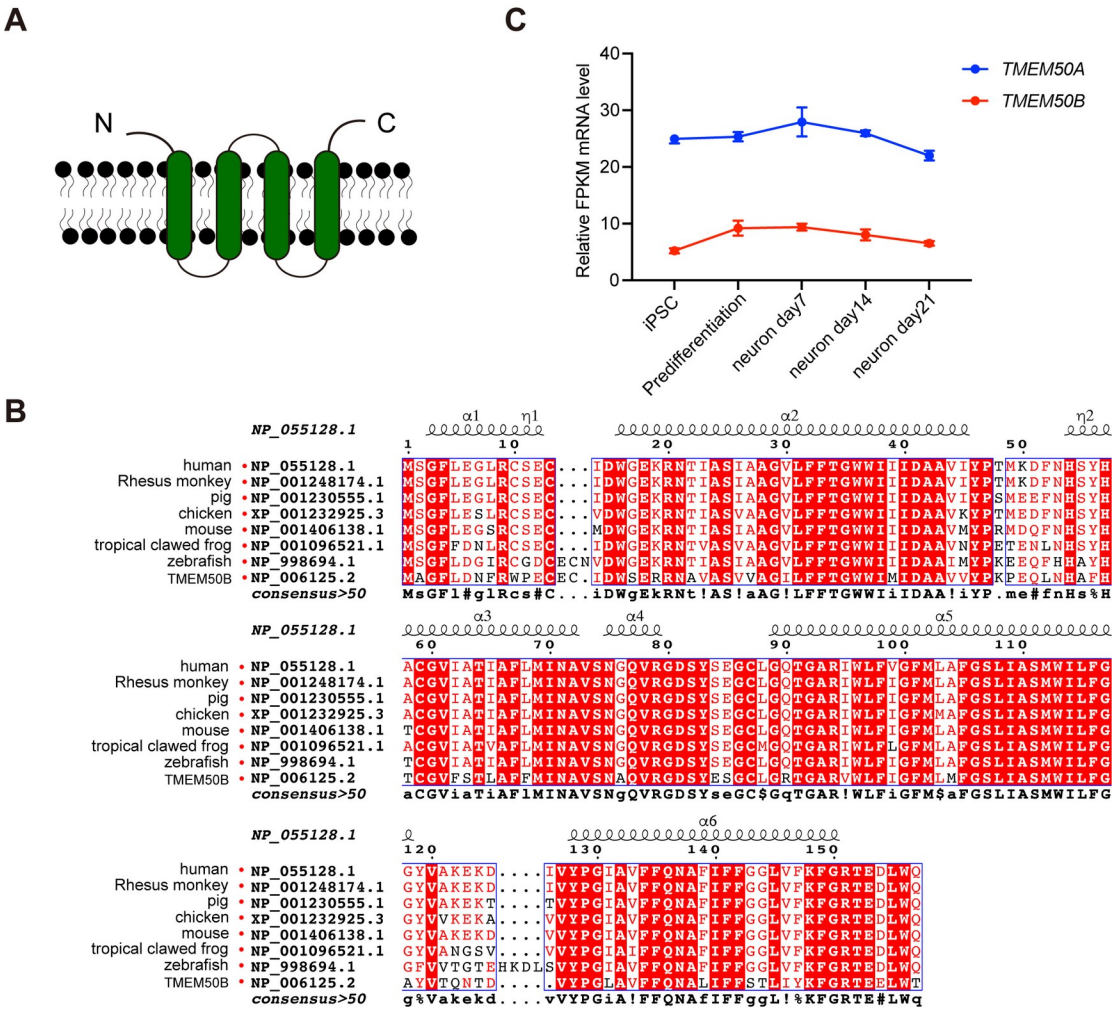

Figure S1. TMEM50A is a conserved four-pass transmembrane protein and is the predominant paralog in iNeurons

(A) Predicted membrane topology model of TMEM50A based on TMHMM analysis[82] showing four transmembrane helices (green) with both N- and C-termini facing the cytosol.

(B) Protein sequence alignment of TMEM50A. The alignment was created with ESPript 3.0 alignment editor. The protein sources and their NCBI accession numbers are indicated. Conserved residues are highlighted in red, and predicted α-helices (α1–α6) are indicated

above the alignment. TMEM50A is highly conserved across vertebrates.

(C) Expression profiles of *TMEM50A* (blue) and *TMEM50B* (red) during iNeuron differentiation, quantified from RNA-seq as relative FPKM. *TMEM50A* is expressed at higher levels than *TMEM50B* at all stages. Data are presented as mean ± SD (n = 3 biological replicates).

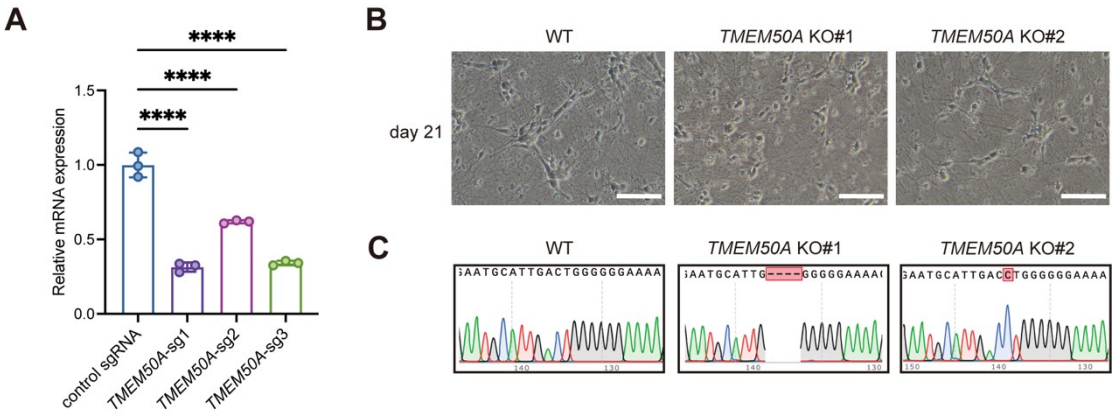

Figure S2. Validation of *TMEM50A* knockdown and KO in iNeurons

(A) RT-qPCR analysis of *TMEM50A* expression in WT and *TMEM50A* knockdown iNeurons. Data are shown as mean ± SD (n = 3). ****p < 0.0001, one-way ANOVA.

(B). Representative phase-contrast images of WT and *TMEM50A* KO iNeurons at Day 21, showing comparable overall neuronal morphology. Scale bars, as indicated.

(C). Sanger sequencing of WT and *TMEM50A* KO iNeurons confirming the genetic knockout in two independent clones (KO#1 and KO#2).

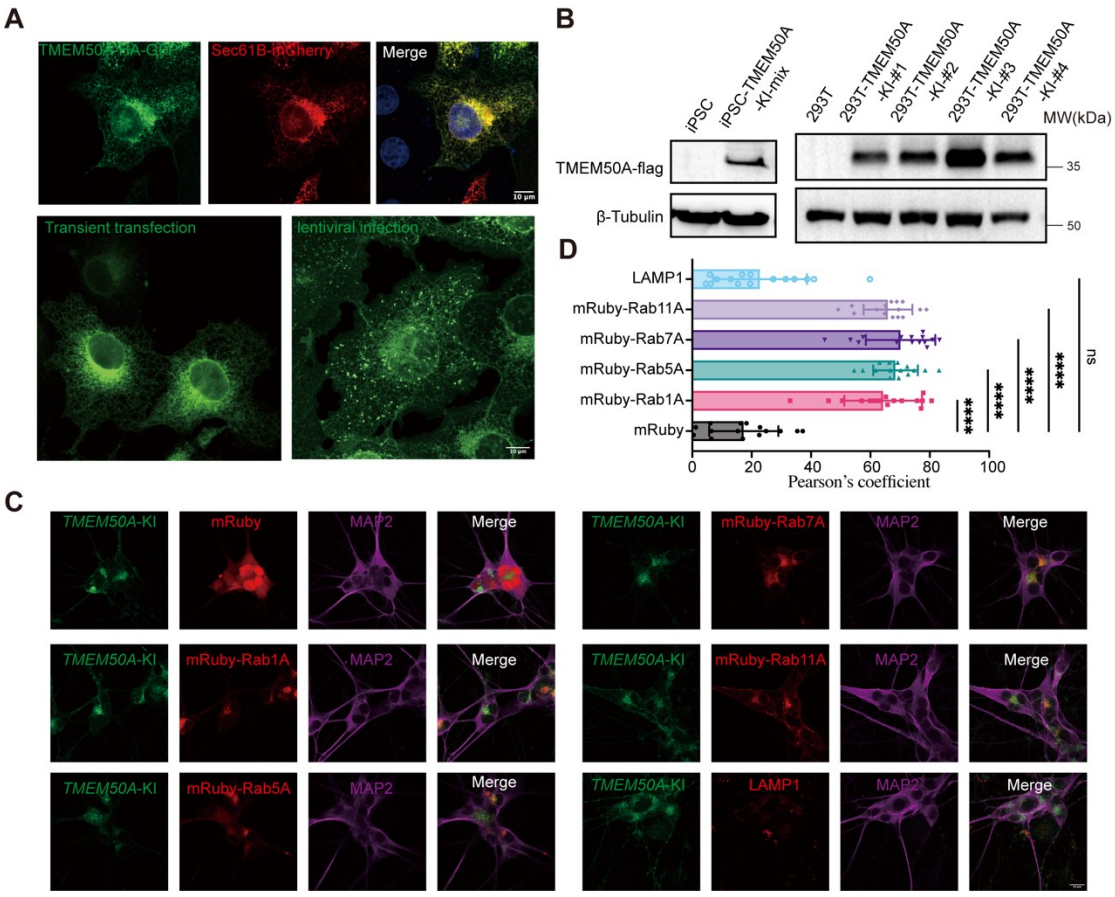

Figure S3. TMEM50A localizes to endosomal compartments but not lysosomes

(A) Localization of exogenously expressed *TMEM50A* is affected by its overexpression levels. transient transfection produces prominent ER/reticular localization (top and bottom left), whereas lower-level lentiviral expression reveals predominantly punctate/vesicular *TMEM50A* distribution (bottom right). Scale bars, 10 μm.

(B) Western blot validation of *TMEM50A*-3×FLAG-mNeonGreen KI in hiPSCs and HEK293T cells with anti-Flag antibody.

(C) Representative immunofluorescence images of *TMEM50A*–KI iNeurons (green) with endosomal and lysosomal markers as indicated (red) and stained for MAP2 (purple). Scale bar, 10 μm.

(D) Quantification of co-localization between *TMEM50A*–KI and

indicated compartment markers using Pearson's correlation coefficient. Data are shown as mean ± SD (n = 15 imaging fields). ns, not significant. ****$p < 0.0001$, one-way ANOVA.

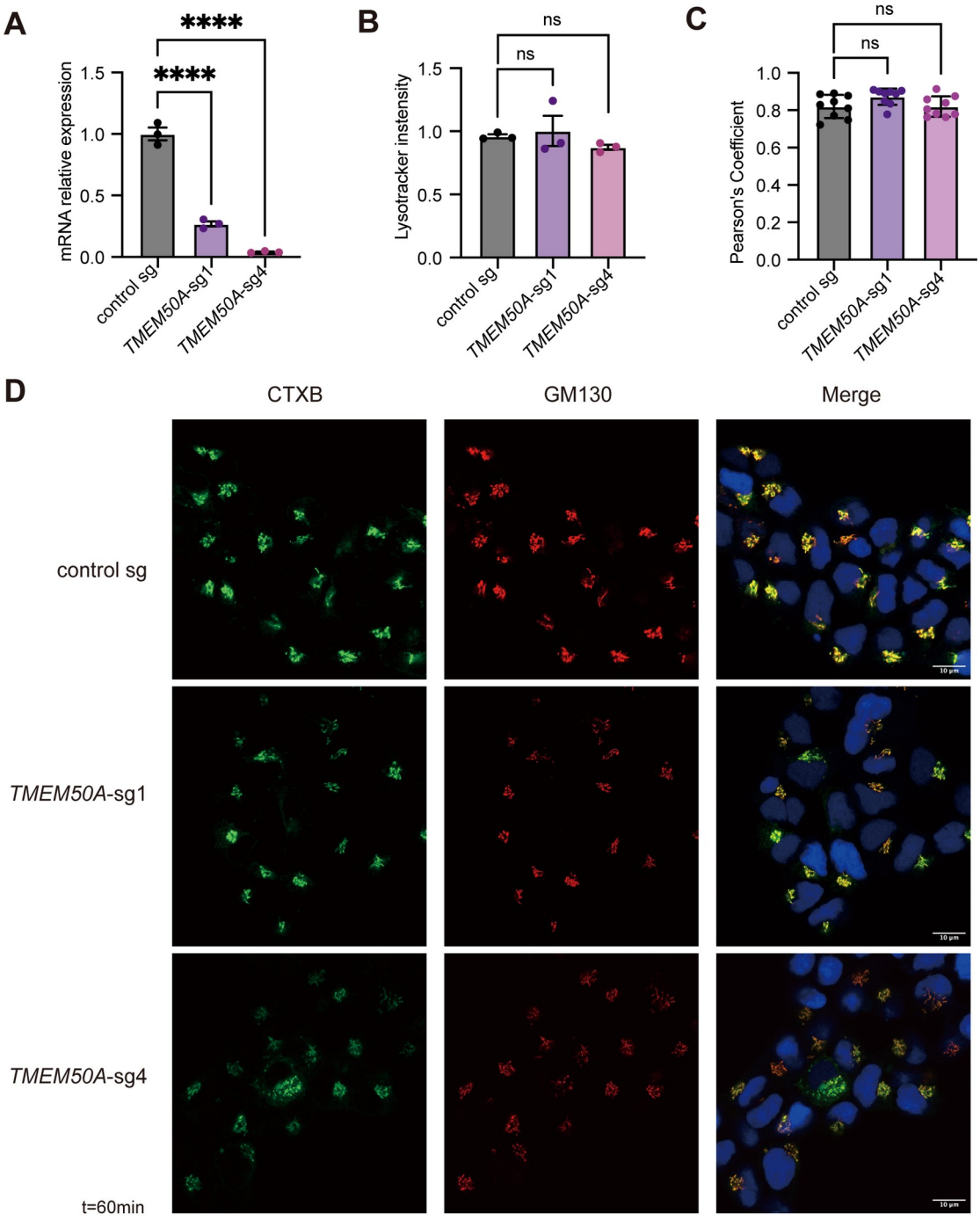

Figure S4. *TMEM50A* knockdown does not disrupt lysosomal integrity or retrograde transport

(A) qRT–PCR analysis confirming efficient *TMEM50A* knockdown in HEK293T cells expressing two independents *TMEM50A*-targeting sgRNAs (*TMEM50A*-sg1, *TMEM50A*-sg4) compared with control sgRNA. Data are presented as mean ± SD (n = 3 technical

replicates). ****$p < 0.0001$, one-way ANOVA.
(B) Quantification of LysoTracker fluorescence intensity in control and *TMEM50A*-knockdown HEK293T cells. Data are mean ± SD (n = 3 technical replicates). ns, not significant, one-way ANOVA.
(C) Quantification of the Pearson's correlation coefficient measuring colocalization of GM130 and CTxB. Data are mean ± SD (n = 8 imaging fields). ns, not significant, one-way ANOVA.
(D) Representative confocal images of CTxB (green) and GM130 (red) in control and *TMEM50A*-knockdown HEK293T cells after a 60-min chase, with nuclei stained by DAPI (blue). Scale bar, 10 μm.

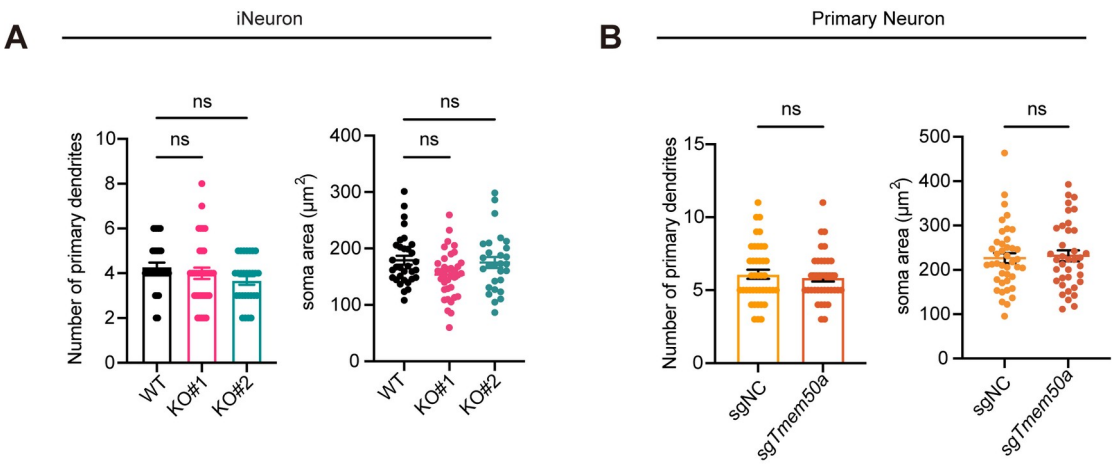

Figure S5. TMEM50A loss does not affect neuronal morphology

Quantifications of number of primary dendrites and soma area in iNeurons (A) (WT n=32, KO#1 n=36, KO#2 n=28, ns, not significant, one-way ANOVA) and primary mouse neurons (B) (sgNC n=41, sg *Tmem50a*=37, ns, not significant, unpaired t test). Data was analysed using same confocal images from Figure 5&6.